Direct Dark Matter Detection using Liquid Xenon Detectors

· U  C ·

Edward Santos

Department of Physics

University of Coimbra

A thesis submitted for the degree of

Master in Physics

24/07/2010

To my grandparents.

Acknowledgements

Graduating has been a long, extenuating run. No matter how joyfully I tried to take every task I underwent during these years, it would have been much harder if I could not count with the support of a few people who surround me, only some of whom it is possible to mention here, where I wish to pay my tribute to them.

With my supervisor, Dr. Vitaly Chepel, I grew as a physicist. I thank him for guiding me through the workmanship of this thesis and in the writing of my first publication. His is a style I admire, and his is the recognition I want to obtain above any other. Besides physics, he though me, through his example, values I must retain for my carer, such as uprightness.

I would like to leave a warmful greeting to my office partners and friends, Drs. Alexandre Lindote, Filipa Balau, Francisco Neves, Luiz de Viveiros and Vladimir Solovov. We had a wonderful year together. I am happy for having their friendship and I am truly thankful to them for enduring me everyday. I have benefit from their skills and knowledge many times, having nothing to give in return but my appreciation. I am also very thankful to Dr. Alessio Mangiarotti and Dr. Brigitte Hiller for helpful discussions along this year, and for their never-ending kindness. I am also thankful to Dr. Isabel Lopes, who has been a very good influence in my carer and has always helped me to make important decisions.

As this is the end of a five year journey in the Physics Department of the University of Coimbra, I feel this is also the place to thank Dr.

Rui Ferreira Marques. We met when I was still a High School student, during a Summer project. It was this experience that compelled me to undergo the Physics course in Coimbra, that I am now ending. For this experience I am also thankful to Dr. Paulo Fonte and his crew. I also acknowledge LIP-Coimbra for giving me the opportunity to experience scientific research since my first years in college.

A final cheer goes to my caring family and to my dear friends: Miguel Fiolhais, Susana Santos, Inês Ochoa, João Campos and, especially, Lúcia Fonseca. These last years would not have been the same without them.

Abstract

The writting of this thesis was motivated by difficulties arising in the operation of dual-phase detectors, which we have been using for dark matter detection. In Chapter 1, the dark matter problem is illustrated and the well-motivated WIMP particle is presented. In Chapter 2, proposed techniques for detection of this particle are discussed. In particular, the ZEPLIN III detector is introduced. This is a dual-phase noble gas detector, that suffers from several difficulties which arise in this general class of detectors. In particular, scintillation efficiency of liquified noble gases is a great matter of discussion among physics community, being not only poorly understood, but having experimental attempts of its measuring shown sometimes contradictory results. This will be the topic of Chapters 3 and 4. In Chapter 5, the topic will be single electron signals arising in the ZEPLIN III detector. Signal description, possible origins and applications are studied. Namely, we study the possibility of using this feature to measure the coherent neutrino-nucleus scattering. This interaction has never been measured. Finally, in Chapter 6, some prospects on the measurement of xenon response with low-energy heavy ions are resumed.

Resumo

A escrita desta tese foi motivada por dificuldades inerentes à operação de detectores dupla-fase, os quais vêm sendo usados na tentativa de detecção de matéria negra.

No Capítulo 1, a problemática da matéria negra é colocada, sendo apresentada a WIMP como partícula candidata. No Capítulo 2, as técnicas propostas para a detecção desta partícula são expostas. Em particular, o ZEPLIN III é apresentado. Este, é um detector dupla-fase com gás nobre, que está sujeito a problemas dos quais padecem os detectores da mesma classe. Em particular, a eficiência de cintilação dos gases nobres é tema de debate na comunidade especializada, tendo os ensaios experimentais para a sua medição mostrado, por vezes, resultados contraditórios. Este será o tópico dos Capítulos 3 e 4.

No Capítulo 5, o tema será o sinal "single electron" emergente no ZEPLIN III. Será feita a descrição do sinal e a discussão de possíveis origens e utilidade. Nomeadamente, estudamos a possibilidade de usar esta capacidade para efectuar a medição da difusão coerente de neutrinos por núcleo atómicos, processo nunca medido até à data.

Finalmente, no Capítulo 6 são estudadas possibilidades de medição da resposta do xenon a iões lentos e pesados.

Contents

1 Dark Matter in the Universe **1**

1.1 Evidence for Dark Matter . . . 2

1.1.1 Cosmological Observations . . . 2

1.1.1.1 Gravitational Lensing . . . 2

1.1.1.2 Rotational Velocity in Spiral Galaxies . . . 6

1.1.1.3 Anisotropy of the Cosmic Microwave Background 8

1.2 Cosmological Parameters . . . 9

1.3 Cold and Hot Dark Matter . . . 10

1.4 Dark Matter Candidates . . . 10

1.4.1 SUSY Theory . . . 11

1.4.1.1 The Neutralino . . . 16

1.4.2 Other candidates . . . 16

1.4.2.1 Baryonic Dark Matter . . . 16

1.4.2.2 Neutrinos . . . 16

1.4.2.3 Kaluza-Klein dark matter . . . 17

1.4.2.4 The Axion . . . 17

2 Dark Matter Detection **18**

2.1 Indirect Detection . . . 18

2.2 Direct Detection . . . 19

2.3 The ZEPLIN III Program . . . 23

2.3.1 Detector Concept . . . 25

2.3.2 Signal Production and Discrimination . . . 26

2.3.3 Other interesting features . . . 28

2.3.4 Position Reconstruction . . . 29

2.3.5 Energy Reconstruction 30

3 Quenching of Scintillation light for Nuclear Recoils 32
3.1 Lindhard theory of Energy Loss 33
3.2 Electronic Quenching 34
3.2.1 Dependence of Scintillation Yield on LET 34
3.2.2 Birks Saturation Law 35
3.2.3 Hitachi's Treatment 36

4 Simulation of the Interaction of Low-Energy Ions with Matter 38
4.1 GEANT4 38
4.1.1 Electronic Stopping - G4IonIonization 39
4.1.1.1 Models and Parametrizations 40
4.1.2 Nuclear Stopping - G4ScreenedNuclearRecoil 41
4.1.3 Validation 42
4.1.3.1 α-particle in Water 42
4.1.3.2 Xenon Ion in Liquid Xenon volume 43
4.1.3.3 Argon Ion in Liquid Argon volume 43
4.2 Scintillation Efficiency Estimations 43

5 The Single Electron Signal 48
5.1 Signal Estimation 49
5.2 The SE dedicated run 50
5.2.1 Description 50
5.2.2 Results 51
5.3 The First Science Run Contributions 57
5.4 Origins of the Signal 57
5.5 Importance of the Single Electron signal 59
5.5.1 Coherent Neutrino Scattering 59
5.5.1.1 The process 60
5.5.1.2 Rate Estimation 60

6 Prospects for Measurements of Xenon Response with Low-energy Ions **66**
6.1 Objectives 66
6.2 Existing Experience with Scintillation Crystals 67
6.2.1 Simulation of the Ion Passage Through Si_3N_4 Windows . . 67
6.3 Conclusions 68

7 Conclusion **73**

A Appdx A **75**
A.1 Ziegler's Scientific Citations for Xenon 75

B Appdx B **82**
B.1 Nuclear Screening Functions 82
B.1.1 Moliere Screening 82
B.1.2 Lenz-Jensen Screening 83
B.1.3 ZBL Screening 83
B.1.4 LJZBL Screening 83

C Appdx C **84**
C.1 Effective Charge Calculation 84

References **89**

List of Figures

1.1 The quintuplicated image of a distant quasar. *Image credit: NASA.* 3
1.2 Some examples of Einstein lensing. *Image credit: NASA.* 4
1.3 As one looks into the distance, one looks back through time, virtue of the finite speed of light. Looking to a set of slices at fixed distances (top), COSMOS group was able to construct a 3-D map (bottom) that ilustrates dark matter distribution through time. Evolving over time from right to left, the distribution of dark matter seems to be clustering. *Image credit: NASA.* 5
1.4 Separation of dark matter (blue region) from baryonic matter (red) in a cluster collision. *Image credit: NASA's Chandra X-ray Observatory and Hubble Space Telescope.* 6
1.5 Variation of the rotational velocity of stars in the NGC 3198 galaxy along the distance to the centre of the galaxy. Expected velocity variations for halo and disk distributions of matter are also shown. The data points seem to be well described by a sum of both functions. 7
1.6 WMAP all sky map of temperature anisotropies. 9
1.7 The Higgs field (assuming positive μ^2 and λ). 12
1.8 Loop correction for Higgs vev - contribution ariving from a Standard Model fermion. 12
1.9 Loop correction for Higgs vev - contribution ariving from a new scalar particle. 13
1.10 Intersection of the running coupling constants occurs in the MSSM. This is a feature the SM is not able to produce. 15

2.1 Expected recoil energy spectra of a $100 GeV c^{-2}$ WIMP in several target species. Dashed lines show the total integrated event rate above a given threshold. The exponential decrease of the integrated event rate with the recoil energy makes low-threshold a crucial requirement for dark matter detectors. 21
2.2 Exclusion limits for several experiments and favored region in the parameter space for the apperance of the SUSY dark matter particle. 24
2.3 Engineering scheme of ZEPLIN III detector. Liquid nitrogen is used to refrigerate the detector, keeping the xenon (blue region just above the PMTs) in the liquid phase. *Courtesy of the ZEPLIN Colaboration.* 25
2.4 Illustration of signal formation in the ZEPLIN III detector. The primary scintillation is formed in the liquid (S1); some ionization electrons drift to the gaseous phase where the secondary scintillation is created. In the bottom right, a representation is shown of the typical signal delivered by the array of PMTs. Features as time separation between S1 and S2 and time extension of both signals are represented. 27
2.5 Example of two signals in ZEPLIN III, after a xenon recoil. The upper trace corresponds to the scattering of a neutron and the lower one to a γ-ray. *Image credit: ZEPLIN Collaboration.* 28
2.6 Scintillation yield for Xe, Ar and NaI(Tl) dependence on LET for a variety of impinging particles. W_{ph} represents the energy necessary to extract a photon from the atomic medium. Extracted from [(1)] 31

3.1 Fraction of the electronic losses of argon and xenon ions in the respective liquid. 35

4.1 Nuclear screening functions. 42
4.2 Bragg curve for 5.49 MeV alpha-particle in water. 43
4.3 Xenon range in a liquid xenon target. 44
4.4 Argon range in liquid argon target. 44
4.5 Argon $\mathcal{L}_{eff}$ as simulated by GEANT4 and compared to existing measurements. 46

4.6 Xenon $\mathcal{L}_{eff}$ as simulated by GEANT4 and compared to existing measurements. 47

5.1 Waveform with two single electron clusters. In the zoom, one can see the individual photo-electron pulses that build the signal. . . . 50
5.2 Number of photoelectrons in the Single Electron signal, using individual peak counting. 51
5.3 Number of photoelectrons in the Single Electron signal, using the area integration method. 52
5.4 Radial coordinates of single electron events. 53
5.5 Radial distribution of single events though the detector. 53
5.6 Duration of the single electron signal. 54
5.7 Variation of the cluster duration along the detector radius. 55
5.8 Clear separation between noise population (bottom, right) and SE peak-events (at the center). 56
5.9 The cluster duration plotted against the number of photolectrons in the cluster also shows clear separation between noise and SE population 56
5.10 Depth of single electron events in the First Science Run. 58
5.11 CNS cross-section for interaction with different target species. . . 61
5.12 Maximum energy deposition in a coherent neutrino-nucleus scattering with different target species. 61
5.13 Expected count rate, computed from the quantities in figures 5.11 and 5.12. Note this is not an actual event rate: multiplication by the neutrino flux is required first. 62
5.14 Number of events after one year run. The single-electron peak (red) is only due to spontaneous SE events in the detector. The blue curve is the two-electron peak from neutrino events. The dashed line shows the 5σ threshold above the mean of the SE distribution. 64

6.1 Schematic representation of the geometry of the simulation. . . . 68

6.2 Energy and momentum dispersion for 300 keV Xe ion after transposing a 100 nm thick Si_3N_4 window. Transmission efficiency: 17.9%. 69
6.3 Energy and momentum dispersion for 300 keV Xe ion after transposing a 100 nm thick Si_3N_4 window. Transmission efficiency: 92.8%. 69
6.4 Energy dispersion for 150 keV Xe ion after transposing a 30 nm thick Si_3N_4 window (detail). 70
6.5 Energy and momentum dispersion for 75 keV Xe ion after transposing a 30 nm thick Si_3N_4 window. Transmission efficiency: 33.8%. 70
6.6 Energy and momentum dispersion for 50 keV Xe ion after transposing a 30 nm thick Si_3N_4 window. Transmission efficiency: 51.9%. 71
6.7 Energy and momentum dispersion for 75 keV Xe ion after transposing a 20 nm thick Si_3N_4 window. Transmission efficiency: 86.7%. 71

Chapter 1

Dark Matter in the Universe

To know what the Universe is made of is an ancient design of Man. In the twentieth century, particle physics and cosmology have been very successful in extending our knowledge about the fundamental components and origin of the material world we see. A consistent description of the Universe and its parts has been achieved, satisfying in part our curiosity. Still, some observations we make are still escaping from the light of our comprehension.

A wide variety of particles has been found, since the early nineteenth century. We can talk about a "particle Zoo", composed of various kinds of particles that have been categorized and associated in families. First, came the electron, then the proton, and soon there were the first antiparticles, the pions and so on. From all of them, only about a dozen are supposed to be fundamental (i.e., non-divisible): the leptons, the quarks and the force carriers. This general picture, with the four interaction forces through which particles "see" each other builds the Standard Model - the theory of everything we now. But evidence has been building up that the Standard Model might not be everything there is. Inconsistencies in the theory, precision measurements that disagree with theoretical predictions are problems that can not be ignored. Furthermore, observation of the Universe suggests that it is composed in a significant fraction by some uncharted kind of matter - "*the "particle Zoo" is not complete.* In this section we shall refer to the cosmological evidence for the existence of this furtive "dark matter". Furthermore, particle candidates to account for it are suggested.

1.1 Evidence for Dark Matter

Even though gravity is much weaker than the other fundamental forces, it is absolutely decisive for the evolution of the Universe. In this section, we will explore how our current understanding of the evolution and dynamics of galactic structures demand for the existence of still undiscovered form of matter, which must account for the majority of the material density of the Universe.

1.1.1 Cosmological Observations

The existence of dark matter was inferred for the first time in 1933, by physicist and astronomer Fritz Zwicky, who coined the term. He measured the mass of the Coma galaxy cluster using the Virial Theorem, which relates the time-averaged total kinetic energy (T) with the potential energy (V) in a closed, stable system of self-gravitating massive objects. It states that the potential energy must equal the kinetic energy within a factor of two: $2T + V = 0$. After measuring the dispersion velocities of the galaxies in the cluster, Zwicky found that these were to high, when compared to the the mass of the cluster (estimated by photometric methods), in order to build a stable system. This reasoning lead Zwicky to propose that the measurement of the cluster's mass had a flaw, that there was non-luminous matter that was not being accounted for in photometry. He called this non-luminous matter "*Dunkle Matterie*":

> "There is dark matter, matter that can't be directly observed, but whose existence we can infer indirectly, due to its gravitational influence in visible matter."

In other words, Zwicky relied on dark matter to provide the "glue" that kept the cluster together. He further suggested that gravitational lensing could be used to measure the true cluster mass.

1.1.1.1 Gravitational Lensing

General Relativity tells us that, while crossing the Universe, light follows geodesic lines in the space-time fabric which matter curves. This means that the observation of faraway objects can be affected by optical aberrations, if the light has

found a zone in its path that was distorted by an intermediate massive body. The magnitude of the distortion is variable, from distortions that don't affect the shape to distortions that include the appearance of multiple images of the object (figure 1.1) and Einstein rings (figure 1.2).

Figure 1.1: The quintuplicated image of a distant quasar. *Image credit: NASA.*

The study of gravitational lensing is of major importance in astrophysics and in modern cosmology and can be used to reconstruct the mass distribution that originated the distortion. Several projects have studied this effect (for instants, CLASS [(2)], COSMOS [(3)] and MACHO [(4)]) providing information about, not only the mass required for the distortion, but also about the properties of the matter that has generated it. *The striking conclusion has always been that baryonic matter represents a small fraction of the total matter content that is required.*

As a good example, in 2006, the COSMOS[1] group released the result of a 140-day survey of a portion of the sky equivalent to nine angular perimeters of the moon. Exploring their data, they were able to project dark matter distribution through time (figure 1.3).

[1] Cosmic Evolution Survey

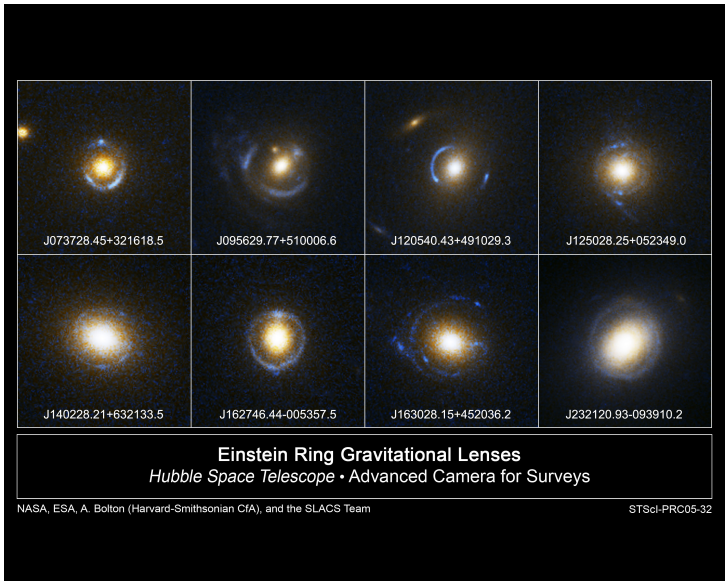

Figure 1.2: Some examples of Einstein lensing. *Image credit: NASA.*

Notable results have also been achieved from observation of two colliding clusters of galaxies, known as Bullet cluster. In this titanic collision, normal matter and dark matter are supposed to behave differently, because dark matter is presumed to be *collisionless* (section 1.1.1.2 extends this discussion). Stars and other forms of visible matter aren't greatly affected by the collision, passing right through most of the time, being only slowed by the gravitational pull. Gases in the two colliding structures, in their turn, represent most of the baryonic mass and can be seen in x-ray photos. They interact electromagnetically and are slowed much more than the stars. As for dark matter, its distribution is determined through gravitational lensing of background objects. The distribution derived from the gravitational lensing cannot be explained by theories without dark matter (like Modified Newtonian Dynamics) because that distribution does not follow the baryonic matter one. The lensing is strongest in two separated regions near the visible galaxies, lying ahead of the collisional gas. This supports the idea that most of the mass of the cluster pair is in the form of collisionless dark matter. This separation of dark matter from normal matter is also presented in the study of another pair of colliding clusters, this time, the MACS_J0025_4–1222.

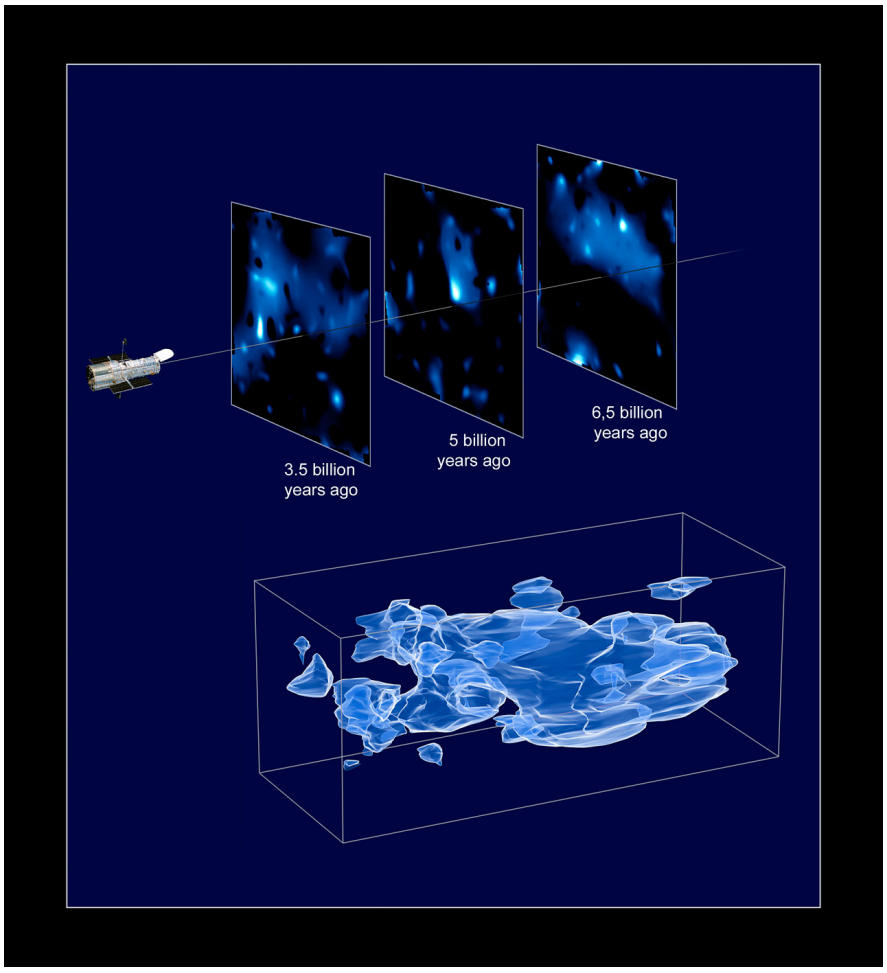

Figure 1.3: As one looks into the distance, one looks back through time, virtue of the finite speed of light. Looking to a set of slices at fixed distances (top), COSMOS group was able to construct a 3-D map (bottom) that ilustrates dark matter distribution through time. Evolving over time from right to left, the distribution of dark matter seems to be clustering. *Image credit: NASA.*

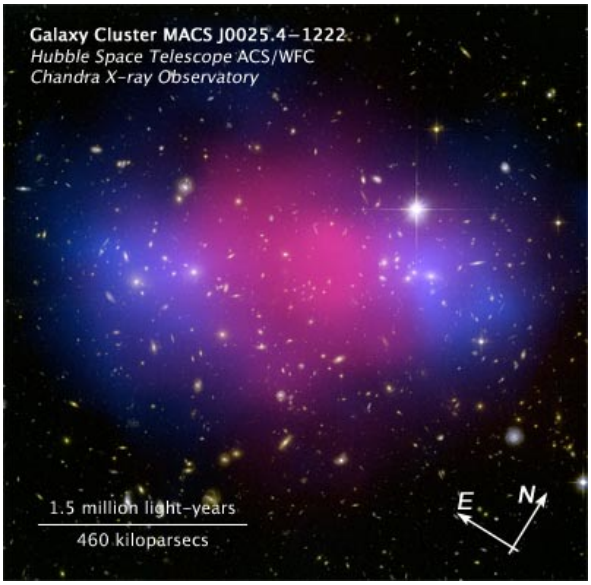

Figure 1.4: Separation of dark matter (blue region) from baryonic matter (red) in a cluster collision. *Image credit: NASA's Chandra X-ray Observatory and Hubble Space Telescope.*

Reconstructing the distribution of all elements in the same way as for the Bullet cluster, the dark matter component is found to lay in the blue region of figure 1.4, while normal matter resides in the red one.

1.1.1.2 Rotational Velocity in Spiral Galaxies

Measurement of rotational velocity in spiral galaxies was first achieved by Vera Rubin in the seventies [(5)] offering very convincing evidence for dark matter. The orbital velocity of a star at a distance r from the center was expected to follow Kepler's third law:

$$v\left(r\right) \approx \sqrt{\frac{GM}{r}} \tag{1.1}$$

where G is Newton's gravitational constant and M is the mass of the galaxy. The velocity of the star would thus depend on the inverse square root of its distance to the center. This is the characteristic rotation curve labeled "disk"

in figure 1.5. However, numerous observations show rotation curves maintaining constant velocities up to galaxy edges.

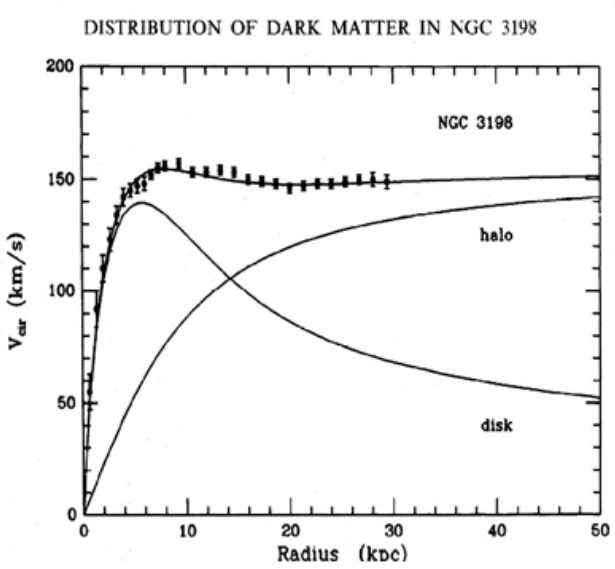

Figure 1.5: Variation of the rotational velocity of stars in the NGC 3198 galaxy along the distance to the centre of the galaxy. Expected velocity variations for halo and disk distributions of matter are also shown. The data points seem to be well described by a sum of both functions.

With exception of theories that modify our current understanding of gravity (which we have already rejected in the previous section), the observed rotation curves can only be explained with the introduction of a spherical halo of dark matter (responsible for a rotation like the one labeled "halo" in figure 1.5). The weight of this dark matter component must account for more than 90% of the mass of the galaxies, if the sum of the "disk" and "halo" curves is to deliver the measured dependency.

The suggestion that dark matter forms halos with an approximately spherical distribution around galaxies, requires that the dark matter particle candidate is collisionless. Otherwise, dark matter would loose it's kinetic energy and settle deep into the galactic gravitational potential wells, forming the galactic disc with

ordinary matter.

1.1.1.3 Anisotropy of the Cosmic Microwave Background

The arguments presented so far illustrate how evidence of the existence of dark matter in the Universe has been, historically, building up. Recently, a dramatical new development has been brought, reinforcing the already solid evidence for dark matter.

The cosmic microwave background, predicted in 1948 and discovered in 1965, is a remaining of the hot Big-Bang. When the expansion cooled the Universe to a temperature below the binding energy of hydrogen, photons decoupled from matter and are still present today, in the microwave region, due to redshift. This ancient radiation fills the Universe, very much in the same sense that a blackbody cavity at a given temperature T is filled with photons. The energy density of the photons is described by the equation

$$\rho = \frac{\pi^2}{15}\frac{(k_B T)^4}{(\hbar c)^3} \tag{1.2}$$

where the characteristic temperature is $T = 2.725 \pm 0,002K$ and Boltzmann's and Planck's constants are $k_B = 1.3807 \times 10^{-23} J/K$ and $\hbar = 1.0546 \times 10^{(-34)} Js$. After Hubble's discovery of the expansion of the Universe, the CMB provides the most convincing evidence of the Big Bang. In 1992, COBE[1] was the first satellite experiment to measure this radiation, showing a remarkable agreement with the black-body spectrum. The isotropy of the CMB radiations supports the idea of an initial homogeneous Universe. Only small perturbations in this homogeneity could exist and further grew due to gravitational attraction, forming the galaxies and clusters we see nowadays. COBE measured these fluctuations to be of order $\Delta T/T \simeq 10^{-5}$. More recently, in 2003, the Wilkinson Microwave Anisotropy Probe (WMAP) improved this measurement. This experiment was sensible enough to detect anisotropies to the 10^{-6} level over angular scales of ~ 7 degrees. Figure 1.6 shows the all sky map of the temperature anisotropies.

The interesting point about the WMAP result is that the measured anisotropy is not enough to develop the current structures we know in the Universe. Since

[1] Cosmic Background Explorer

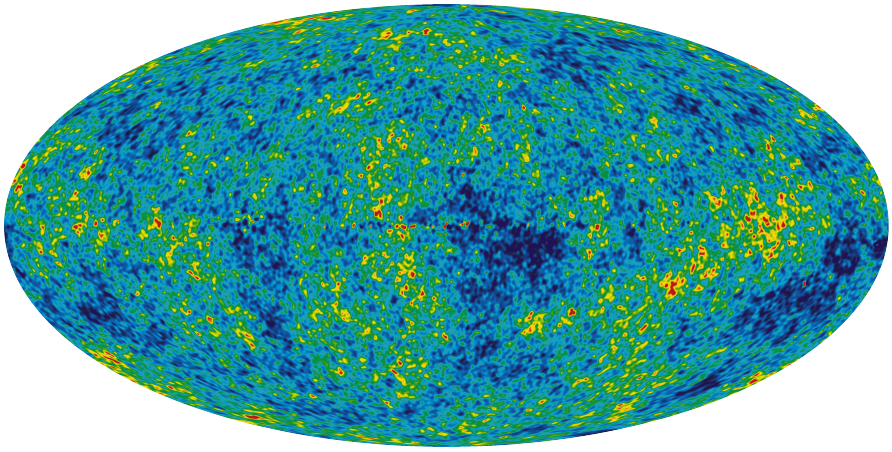

Figure 1.6: WMAP all sky map of temperature anisotropies.

photons only interact with baryonic matter, we can propose that there was dark matter in the early Universe contributing with the missing anisotropy. In this interpretation, dark matter created the gravitational wells where baryonic matter grouped.

1.2 Cosmological Parameters

Dark matter studies started with Fritz Zwicky suggesting that it was "gluing" the Coma cluster; nowadays, in a broadening view, one can find that it is in fact gluing the whole Cosmos. Indeed, dark matter seems to play an important part if one is to answer fundamental question as "how old is the Universe?" or "what is its future?", because these are all question related with the density of the Universe, Ω.

Combination of the study of the Cosmic Microwave Background with other astronomical measurements, allows to predict the cosmological densities of the different components of the Universe. The total matter and energy density of the Universe can be written as:

$$\Omega_0 = \Omega_\Lambda + \Omega_b + \Omega_{DM} = 1.003^{+0.013}_{-0.017}$$

Such a formulation constitutes the ΛCDM model. The first term corresponds

to the vacuum energy. This contribution is commonly known as Dark Energy [ref] and is supposed to be very significant:$\Omega_\Lambda = 0.76^{+0.04}_{-0.06}$. The following two terms account for the matter contribution. The baryonic component, which accounts for luminous matter (like stars and gases) is only $\Omega_b = 0.042^{+0.003}_{-0.005}$, while the missing non-baryonic dark matter is found to compose around twenty per cent of the Universe: $\Omega_{DM} = 0.20^{+0.02}_{-0.04}$.

1.3 Cold and Hot Dark Matter

The argumentation followed so far, not only demands the existence of dark matter in the Universe, as also constrains its nature. The mere existence of the galactic structures we see nowadays place a constrain.

Dark matter has been labeled as “cold” or “hot” to indicate its dispersion velocity. ”Cold” conjectures that dark matter particles moved non-relativistically at the matter-radiation decoupling time in the early Universe, while “hot” supposes otherwise. The relativistic behavior would compromise galaxy formation, since fast dark matter would not aggregate. A Cold, heavy, dark matter particle instead, would decouple long before baryons and start aggregating earlier. The primary small structures would then be able to grow and form larger ones, just like the ones we see. So, we require the significant part of dark matter to be Cold. Nevertheless, some relativistic particles (like neutrinos) can also be (part of) dark matter.

1.4 Dark Matter Candidates

The evidence for dark matter that has been found constrains the properties of the particle candidates. From the previous subsections, one can conclude that a suitable dark matter particle candidate must be neutral, massive, cold, collisionless and non-baryonic. It must also have the correct relic density and be stable on cosmological time scales. There is no such particle in the Standard Model. So, evidence for existence of a dark matter particle is evidence of physics beyond

the Standard Model. A remarkable coincidence is that such a particle is arising in models that pretend to be an extension to the Standard Model, namely, Super-Symmetry. This theory delivers the most well-accepted candidate, the neutralino, which we will explore in the following sections. Other candidates are also enumerated and briefly discussed.

1.4.1 SUSY Theory

The Standard Model is assumed to be a theory acceptable only in a low-energy regime - the electroweak scale, where our current experiments are situated. So far, it has been a very successful theory, but it is not free of exhibiting a few undesired and even problematic features. One of the unsatisfactory aspects is the absence of coupling unification at the GUT scale. More concerningly, the Standard Model has failed important precision tests. The most relevant of these is related with the anomalous dipolar magnetic moment of the muon, for which the predicted value disagrees from the measured one by 2.3 σ. The anomalous dipolar magnetic moment of the electron is one of the best predicted quantities in the SM. The muon, in the other hand, is much more sensitive to physics beyond the Standard Model. This is due to the fact that loop corrections arriving from diagrams which might contain a given set of new particles are proportional to the electron/muon mass. So, hypothetical *new physics* is much more important for the muon, which is 200 times heavier than the electron.

The questions discussed so far are undesirable, but an even more serious issue arises in the Standard Model: the Hierarchy Problem. Super-Symmetry is introduced precisely to solve this feature. The Hierarchy Problem terms the divergence of every particle mass in the Standard Model framework. More precisely, the divergence appears in the vacuum expectation value of the Higgs field - the minimum of the Higgs potential:

$$V = -\mu^2 \phi^\dagger \phi + \frac{\lambda}{4} \left(\phi^\dagger \phi\right)^2$$

If we assume μ^2 and λ to be positive, the potential will have a non-vanishing minimum located at $\nu = \sqrt{-\mu^2/\lambda}$. Figure 1.7 illustrates this potential, popularly known as the "Mexican hat".

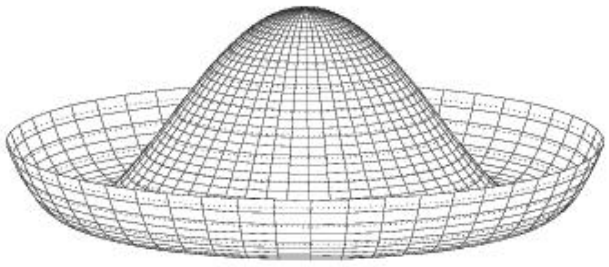

Figure 1.7: The Higgs field (assuming positive μ^2 and λ).

When loop corrections corresponding to diagrams like the one in figure 1.8 are made, the correction found diverges quadratically:

$$\Delta m_H^2 = -\frac{|\lambda_f|^2}{8\pi^2}\Lambda^2 + ...$$

where λ_f denotes the coupling of the Higgs particle to a SM fermion and Λ is some cut-off high-energy constant above which the Standard Model is no longer a valid theory. At most, this will be the scale where a theory of quantum gravitation is necessary, 10^{19} GeV.

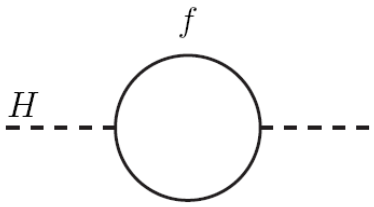

Figure 1.8: Loop correction for Higgs vev - contribution ariving from a Standard Model fermion.

In QED, all particles are massless; they acquire mass through Yukawa interactions, when they couple to the Higgs particle. In this way, the quadratic divergence in the Higgs mass propagates to all particles in the Standard Model. At this point, one might remember how gauge and chiral symmetry control the

divergences in QED and ask if the introduction of a new symmetry could solve the problem. Effectively, that is the solution, being super-symmetry the novelty introduced. Suppose there exists a scalar particle (i.e., spinless) with mass m_S that couples to Higgs according to $\lambda_S S^2 H^2$ (figure 1.9)

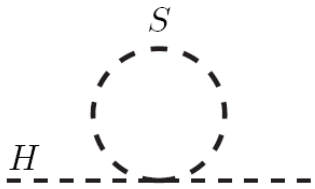

Figure 1.9: Loop correction for Higgs vev - contribution ariving from a new scalar particle.

The loop correction will be

$$\Delta m_H^2 = \frac{\lambda_S}{16\pi^2}\left[\Lambda^2 - 2m_S^2 \ln\left(\frac{\Lambda}{m_S}\right) + ...\right]$$

Summed with the former correction, the overall result is

$$\Delta m_H^2 \sim \left(\lambda_S - |\lambda_f|^2\right)\Lambda^2 + \left(am_S^2 - bm_f^2\right)\ln\Lambda + ...$$

where numeric factors have been disregarded. If we require that the new coupling is $\lambda_S = |\lambda_f|^2$, the quadratic divergence is eliminated. In this sense, the introduction of a symmetry which relates bosons with fermions is the solution. As every fermion in the standard model can play the role of the fermion in diagram 1.8, there will be a super-symmetrical partner for each one of them. There is a logarithmic diverges that is left over, but this is a "safe" divergence:

$$\Delta m_H^2 \propto \left(am_S^2 - bm_f^2\right)\ln\Lambda \tag{1.3}$$

where all numerical factors have been integrated into the constants a and b, which are close to unity. Since SUSY particles were never seen, SUSY must be a broken symmetry (otherwise, SUSY particles would have the same mass as their

Standard Model particle			**Susy partner**		
Name	Symbol	Spin	Name	Symbol	Spin
up-quarks	u, c, t	1/2	up-squarks	$\tilde{u}, \tilde{c}, \tilde{t}$	0
down-quarks	d, s, b		down-squarks	$\tilde{d}, \tilde{s}, \tilde{b}$	
leptons	e,μ, τ		sleptons	$\tilde{e}$,$\tilde{\mu}$, $\tilde{\tau}$	
	ν_e, ν_μ, ν_τ			$\tilde{\nu}_e$, $\tilde{\nu}_\mu$, $\tilde{\nu}_\tau$	
gluons	g	0	gluinos	$\widetilde{g}$	1/2
photon	γ		photino	$\tilde{\gamma}$	
Higgs	(H_u^+, H_u^0)		Higgsinos	$\left(\tilde{H}_u^+, \tilde{H}_u^0\right)$	
	$\left(H_d^0, H_d^-\right)$			$\left(\tilde{H}_d^0, \tilde{H}_d^-\right)$	
W	$W^\pm, W^0$		Winos	$\widetilde{W}^\pm\pm, \widetilde{W}^0$	
B	B		Bino	$\tilde{B}$	
graviton	g	2	gravitino	$\tilde{g}$	3/2

Table 1.1: Particle content of the MSSM.

standard model partners and would have been detected long ago). But, regarding expression (1.3), the difference in the square of the masses can't be too high, or otherwise, a new divergence arises. This limits the mass of the SUSY particles to the $\sim$ 10 TeV range. The Super-Symmetric theory which adds the minimum number of fields to the SM is the Minimal Super-Symmetrical Model (MSSM). Table 1.1 is a comprehensive enumeration of the particle spectrum.

Fermion superpartners are named s-fermions. For instants, the selectron, s-muon, s-tau are SUSY particles. Boson partners are named adding the suffix "ino". The gluino, the higgsino or the wino are examples of this nomenclature. A very pleasant feature of the MSSM is that it allows for unification of the running coupling constants at the a very high energy scale - the GUT scale:

$$\alpha_1 (m_U) = \alpha_2 (m_U) = \alpha_4 (m_U) \equiv \alpha_U$$

SUSY also requires the introduction of a new conserved quantity, called R-Parity and defined as:

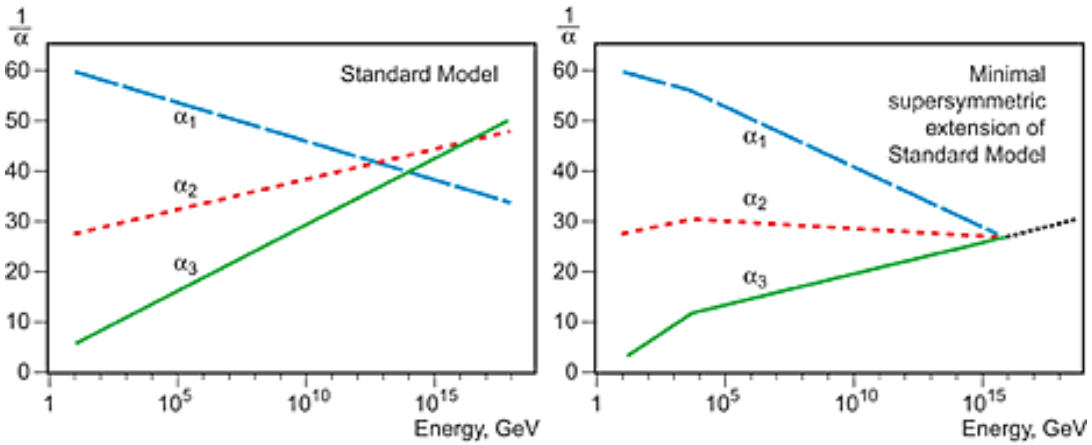

Figure 1.10: Intersection of the running coupling constants occurs in the MSSM. This is a feature the SM is not able to produce.

$$P_R = (-1)^{3(B-L)+2S}$$

This is done in order to preserve baryonic (B) and leptonic number (L). S represents the spin of the particle. One can easily see that every Standard Model particle has $P_R = +1$ and SUSY particles have $P_R = -1$. This has huge implications. For starters, it implies that SUSY particles must be produced in pair, at colliders and every decay of a SUSY particle must always result in an odd number of SUSY particles. Furthermore, it is very important for cosmology because it makes the lightest SUSY particle (LSP) stable: any given SUSY particle can decay to a lighter one until the lightest of all of them is reached. The LSP can not decay into (lighter) SM particles because R-Parity conservation forbids it. If having the right properties, this stable particle is an excellent dark matter candidate.

1.4.1.1 The Neutralino

Calculation of the SUSY particles mass spectrum relies on the definition of 124 parameters, in the unconstrained MSSM. In most cases, the LSP is the lightest neutralino. There are four neutralinos, each one of them a particular superposition of bino, wino and higgsinos quantum states:

$$\tilde{\chi}_i^0 = c_{1i}\tilde{B} + c_{2i}\tilde{W}^3 + c_{3i}\tilde{H}_1^0 + c_{4i}\tilde{H}_2^0$$

The lighter of these states is an excellent candidate for Cold dark matter: it is stable, neutral, and massive. Can be calculated to have the proper density and non-relativistic speed.

1.4.2 Other candidates

Having found the best known candidate, there remain several more proposals. For completeness, we will now make a brief description of these.

1.4.2.1 Baryonic Dark Matter

The existence of baryonic dark matter is not ruled out but it is highly constrained by the CMB anisotropy measurement. As argued in previous sections the baryonic content of the Universe is very restricted: only a small fraction of dark matter can be baryonic. This, is usually assumed to be in the form of MACHOS: Massive Compact Halo Objects, that can be a variety of condensed objects such as black holes, neutron stars, white dwarfs, very faint stars or even planets.

1.4.2.2 Neutrinos

Neutrinos are the best candidates for Hot Dark Matter. They are electrically neutral, very weakly interacting and were recently discovered to have mass. The mass of the two lightest neutrinos are constrained to be very light: $\nu_e < 2.2$ eV and $\nu_\mu < 170$ keV, as the tau-neutrino is still allowed to be relatively heavy ($\nu_e < 15.5$ MeV).

1.4.2.3 Kaluza-Klein dark matter

The Kaluza-Klein theory was proposed in 1921 by the german mathematician Theodor Kaluza. It pretends to unify gravity with electromagnetism by extending general relativity to a five dimensional space-time. In this framework, a set of equations can be separated, leading to Einstein field equations and another set delivers Maxwell's laws of electromagnetism. The lightest Kaluza-Klein excitation can be the dark matter particle if it is electrically neutral. This is usually the the first Kaluza-Klein excitation of the hypercharge gauge boson, $B^{(1)}$. Studies have been made, indicating that such a particle, with a mass in the range of 400 to 1200 GeV could hold a density in agreement with the WMAP measurements [(6)] The Kaluza-Klein dark matter is a well motivated candidate. Experiments that are currently seeking direct or indirect dark matter detection can probe for its existence.

1.4.2.4 The Axion

There is CP violation in the Universe. In the context of the Sakharov Conditions (1967) for a Bariogenesis or a Leptogenesis theory, the processes we known to violate CP symmetry are not enough to warrant for the current matter-antimatter asymmetry. As new sources of CP violation are been searched, a difficult question that arises is why does not the strong force violate CP? This is known as the strong-CP problem in QCD. To solve it, Peccei-Quin theory postulated the existence of a new elementary particle, the axion. In 2006, a claim that the axion had been found was made, but latter deprecated. An italian experiment called PVLAS[1], registered a slight change in the polarization of a laser beam as it passed through a magnetic field in a vacuum. This was interpreted as the result of axion production, when some of the laser beam's photons combined with photons in the vacuum. However, they later found the signal to be an experimental artifact. Furthermore, in 2009 a couple of papers were published, stating that the axion has no motivation to exist, in the sense that its rises a fine tunning problem that is worse that the strong-CP problem that is was invented to solve ([(7)], [(8)]).

[1] Polarizzazione del Vuoto con LASer

Chapter 2

Dark Matter Detection

The answer to weather dark matter exists or not will, ultimately, come from experimental detection. The search for the dark matter particle can be made through three different ways. We can look for its **production** in high energy collider experiments; we can try to detect their **annihilation** products, arriving from distant parts of the Universe; or, we can expect one of these particles to **scatter** in a detector. The last two techniques are labeled Indirect and Direct searches, respectively, and will be explored in this chapter. Naturally, in the context of this work, special attention will be payed to the latter one.

2.1 Indirect Detection

The best dark matter candidate, the neutralino, is likely to be a Majorana particle. Being its own antiparticle, it can annihilate with itself, producing baryonic matter without violating R-Parity. Indirect searches look out for the annihilation products, which can be any number of detectable particles, including neutrinos, $\gamma - rays$, charged leptons, protons and antiprotons. These, are expected to come from regions where the neutralino density is assumed to be greater, due to gravity, like the Sun, the center of Earth or the galactic centers.

The search for $\gamma - rays$ from neutralino annihilation has been attempted by a variety of experiments (FERMI, INTEGRAL, MAGIC). One of them, the EGRET γ-ray telescope has observed an excess of γ-rays, but this was ultimately considered to be a systematic effect.

The $\gamma - ray$ spectrum is expected to be mainly continuum, with a possible mono-energetic feature, arising from annihilation of the type ($\chi\chi \rightarrow \gamma\gamma$). Although the mono-energetic lines are a potential "smoking gun" signature for the existence of dark matter ($E_\gamma \approx m_\chi$), Feynmann dyagrams leading to the γ production have at least one loop, implying small fluxes. For this reason, the search of neutrino fluxes might be more attractive. A detectable flux coming from the sun is expected to have energy substantially higher that solar neutrino energies. ICECUBE [(9)], in the South Pole, and ANTARES [(10)] are searching for this.

Finally, we have experiments searching for antiparticle products. Antiparticles are known to constitute a small fraction of the cosmic-ray flux. They can result from cosmic-ray interaction with interstellar medium or from a primary source (like a pulsar). There are a few reports of an excess in the positron fraction from cosmic rays that have been interpreted by some as a dark matter signature. Using data recorded from 2006 to 2008, the PAMELA[1] satellite-based experiment reported the finding of an excess of positrons. But no excess of antiprotons was found, making the result inconsistent if to be interpreted has dark matter annihilation evidence, since the positron and antiproton excesses are expected to be correlated.

2.2 Direct Detection

A fraction of WIMPS in the early Universe must have annihilated to baryonic matter, otherwise, the remaining abundance would be too high. According to the crossing symmetry, the amplitude for the WIMP annihilation to a given particle is related to the amplitude for elastic scattering from that particle. So, no matter how weak, WIMPS must have some small coupling to baryonic matter (like quarks). This feature is exploited by the experiments attempting direct detection. As the Earth travels through the Universe, a "wind" of WIMPS is constantly passing through it, rarely interacting with the matter that composes the planet.

[1] Payload for Antimatter Matter Exploration and Light-nuclei Astrophysics

A WIMP will either couple to the spin of a nucleus or to its mass. These two channels are referred to as Spin Dependent (SD) and Spin Independent (SI) scattering, respectively. Since WIMPs can have both couplings, the total cross-section will be the sum of the cross-sections for the two interactions. In the scalar (i.e., spinless) interaction, the WIMP scatters elastically from the nucleus as a whole, rather that from a particular nucleon, producing low-energy nuclear recoils. This process is dominant for heavier elements ($A \gtrsim 30$, where A is the number of nucleons), being the enhancement in the cross-section proportional to A^2. On its turn, SD detection can result from elastic (nuclear recoil) or inelastic (level excitation) collisions.
In either SI or SD experiments, the WIMP-nucleon cross-section σ_A, is given by the general expression:

$$\sigma_A = 4G_f^2 \mu_A^2 C_A$$

where G_f is the Fermi weak-coupling constant, the factor μ_A is the reduced mass of the WIMP-nucleon sistem and C_A is a factor which depends on the type of interaction. For the SI interaction, $C_A \propto A^2$, making heavier elements more suitable to build up a detection medium. For the SD case, C_A is related to the nuclear spin J:

$$C_A = \frac{8}{\pi} \left(a_p \langle S_p \rangle + a_n \langle S_n \rangle\right)^2 \frac{J+1}{J}$$

where $a_{n,p}$ are the WIMP-nucleon coupling constants and $S_{n,p}$ are the expectation values for the proton or neutron spins averaged over the entire nucleus.

From the cross-section, one can compute the expected rate for the WIMP-nucleon interaction. The rate per cm^3 of target material is

$$\texttt{Rate} \sim N \frac{\rho_\chi}{m_\chi} \sigma_A v_\chi$$

where N is the number of nuclei in the detector, ρ_χ is the local density of the WIMP particle (estimated to be $\sim 0.3\ GeV/cm^3$), m_χ is its mass and v_χ its local velocity.

As said, enhancement of the spin-independent cross section (usually the dominant component of the interaction) is achieved using heavier target elements,

since it grows with A^2. However, the differential scattering rate also depends on nuclear form factor correction terms. This correction is especially significant for heavy targets, causing a suppression of the differential scattering rate for high recoil energies. The effect is shown in figure 2.1 [(11)].

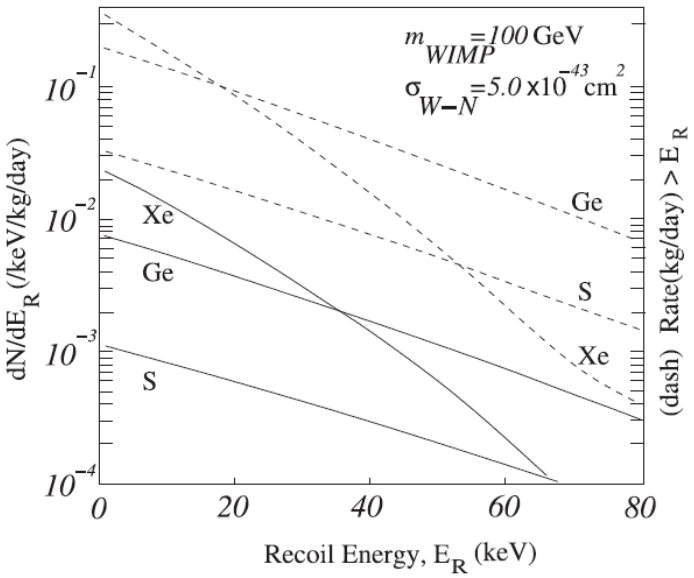

Figure 2.1: Expected recoil energy spectra of a $100 GeV c^{-2}$ WIMP in several target species. Dashed lines show the total integrated event rate above a given threshold. The exponential decrease of the integrated event rate with the recoil energy makes low-threshold a crucial requirement for dark matter detectors.

While in the low recoil energy region the curves are ordered by atomic number, at higher recoils energies the recoil spectrum of Xe is specially suppressed due to the form factor - there is loss of coherence at high momentum transfers. It is also visible the dependence of the integrated event rate on the nuclear recoil energy threshold: this must be as low as possible in order to maximize the detector sensitivity to WIMPs.

As the absolute rates are expected to be lower than 1 $event/day/kg$ of detector, background must be highly suppressed. This requirement is the reason why dark matter seeking detectors are located in underground laboratories. There,

the cosmic ray induced background is attenuated by the rock shielding. Moreover, components of the detector might be a source of background themselves, reason for which they are selected to be extremely radio-pure.

If there is no background the sensitivity of the detector will be directly proportional to the product of its target mass (M) by the exposure time (T). But, if there is background, which is estimated and subtracted from the signal, then the sensitivity is proportional to $\sqrt{MT}$. In this case, the background will limit the sensitivity, which will not improve after some given exposure time limit is reached.

The considerations made so far about cross-sections, event-rate, energy threshold and background reduction concern every experiment aiming at WIMP direct detection.

There are several ways to identify a WIMP scatter, since the energy deposition can produce several measurable signals, such as scintillation, ionization or heating. Most of the existing experiments focus on detection of one or two of these quantities[1]. We can distinguish two main techniques for direct detection: cryogenic detectors and noble gas detectors.

Cryogenic detectors use crystals cooled to mK temperatures to measure the energy that is transfered to lattice vibrations (phonons). The heat measurement can be combined with that of another excitation channel (ionization or scintillation), allowing to achieve great discrimination capability (as the ratio of the second channel to the phonon one will provide the discrimination). CRESST measures phonons and scintillation; EDELWEISS and CDMS[2], in their turn, measure phonons and ionization.

The cryogenic experiments have shown great discrimination, energy resolution and low energy thresholds. Still, they have some drawbacks. They are sensitive

[1]There are also a few experiments relying on the detection of WIMPS through superheated droplet detectors[(12)], such as PICASSO [(13)] and SIMPLE [(14)].

[2]The Cryogenic Dark Matter Search, as shown in figure 2.2, holds the best exclusion limit for direct dark matter detection.

to surface contamination. The interaction rate is also an issue. This rate depends on the A of the target material and the mass of the detector. Typical cryogenic targets (Ge, Si) are lighter than Xe, used in noble gas detectors. Furthermore, high-purity crystals are neither easy nor cheap to produce, being each detector limited to a few hundred grams. Hence, in order to achieve a large target mass, many modules are required, increasing the complexity, cost, and background within the cryostat, which are a problem themselves, adding long cooling/warming times to the length of commissioning periods.

In their turn, noble gases represent a cheaper target, making them very attractive as detection media [(15)]. Indeed, they are available in large amounts as byproducts of steel industry. Furthermore, noble gases can be relatively easily purified. Dark matter seeking experiments of this class include the ZEPLIN[1][2] detectors ([(16)], [(17)], [(18)]) and XENON10 [(19)]. In particular, ZEPLIN II [(17)] published the first dark matter search result from a two-phase noble gas detector. Several more experiments of this class are being planned in the ton mass scale, like the XENON1T [(20)] or ArDM [(21)]. Further details about dual-phase detectors operation will be given in the following sections as we will focus on the ZEPLIN III detector.

2.3 The ZEPLIN III Program

In the ambit of direct searches, several experiments arise all over the world, trying to detect the scatter of a WIMP particle. ZEPLIN III is one of the leading experiments in the area. Located 1.1 km underground in Boulby, UK, it measures both ionization and scintillation arising from an interaction in its liquid xenon target.

[1] ZonEd Proportional scintillation in LIquid Noble gases
[2] ZonEd Proportional scintillation in LIquid Noble gases

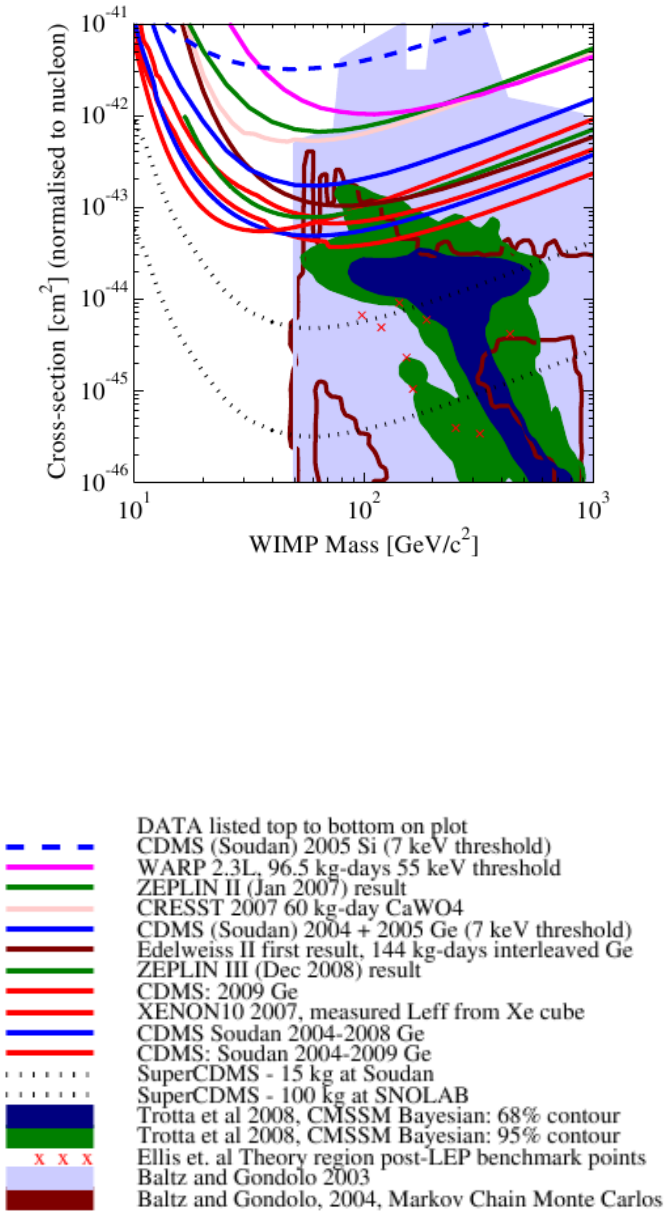

Figure 2.2: Exclusion limits for several experiments and favored region in the parameter space for the apperance of the SUSY dark matter particle.

2.3.1 Detector Concept

ZEPLIN III is a two-phase (liquid/gas) xenon detector. It has a 12 kg liquid target-disc, ≈40 mm thick and 160 cm radius, in equilibrium with a 5 mm tick gaseous phase. A 31 PMT array collects light providing from the detection media. Figure 2.3 shows the engineering scheme of the detector.

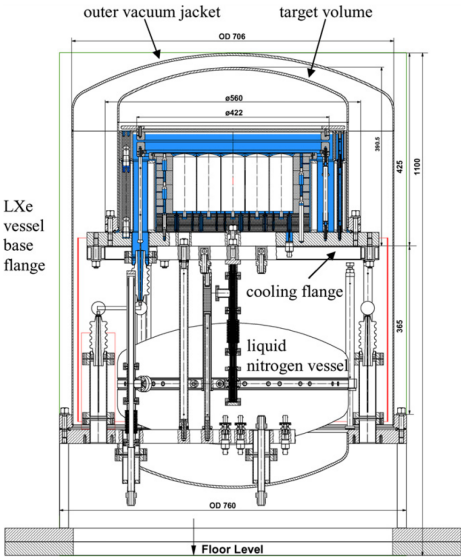

Figure 2.3: Engineering scheme of ZEPLIN III detector. Liquid nitrogen is used to refrigerate the detector, keeping the xenon (blue region just above the PMTs) in the liquid phase. *Courtesy of the ZEPLIN Colaboration.*

When a particle interaction occurs in the detector, excited and ionized xenon atoms are formed. Scintillation is produced by excited xenon dimers (Xe_2^*), which are formed from excited (Xe^*) and ionized Xe_2^+ states. For the excited xenon atoms, light production takes two steps. First, the exciton collides with a ground state, forming an excited molecule (the excimer), which then de-excitates emitting a photon:

$$Xe^* + Xe \rightarrow Xe_2^*$$

$$Xe_2^* \rightarrow 2Xe + h\nu$$

where $h\nu$ is the energy of the scintillation photon. As for the ionized atoms, they are converted into excited states through a recombination process

$$Xe^+ + Xe \rightarrow Xe_2^+$$

$$Xe_2^+ + e \rightarrow Xe^{**} + Xe$$

$$Xe^{**} \rightarrow Xe^* + heat$$

before de-excitation by the process already described above. These two mechanisms are called the excitation and recombination components of the scintillation. The scintillation light is produced in transitions from the two lowest states of Xe_2^* molecule, the singlet $^1\Sigma_u^+\,(1_u)$ and the triplet $^3\Sigma_u^+\,(0_u^+)$, to the dissociative ground state $^1\Sigma_g^+\,\left(0_g^+\right)$. The resulting emission lies in the vacuum ultraviolet (VUV) region and has a continuous spectrum centered at 178 nm with FWHM of 14 nm [(22)]. The excitation component leads to light emission in 2.2 ns while the recombination component takes 27 ns. This prompt scintillation forms the primary scintillation signal, already labeled S1, above.

Applying an electric field, some of the ionization electrons can be removed from the interaction site. These electrons further drift into the gaseous phase where they are accelerated (in the gas, the electric field is twice as strong, given that the dielectric constant of liquid xenon is ≈ 2) and produce secondary scintillation through inelastic collisions with xenon atoms. This secondary scintillation (typically termed S2 by the specialized community) will have a time duration proportional to the gaseous phase thickness (and inversely proportional to the time the electron takes to cross the whole depth). These concepts are illustrated in figure 2.4.

2.3.2 Signal Production and Discrimination

In ZEPLIN III, the strong electric field prevents some electrons from recombining and extracts them to the gaseous phase, where the secondary scintillation signals is formed. The efficiency of the extraction of the electrons from the track depends on the LET (Linear Energy Transfer) of the incident particle, i.e., on the energy deposited per unit of path length. Strongly ionizing particles produce tracks with

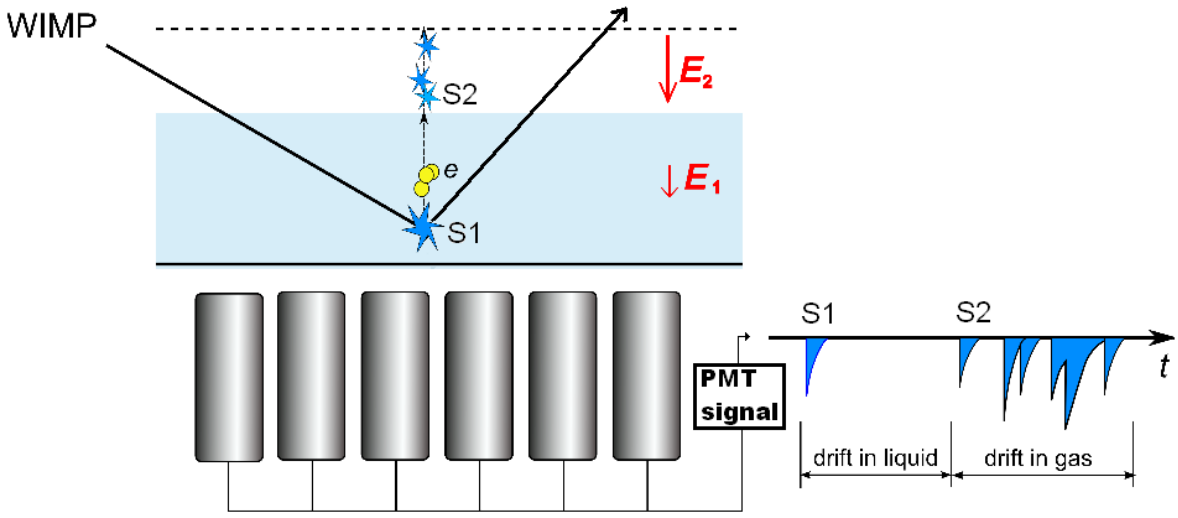

Figure 2.4: Illustration of signal formation in the ZEPLIN III detector. The primary scintillation is formed in the liquid (S1); some ionization electrons drift to the gaseous phase where the secondary scintillation is created. In the bottom right, a representation is shown of the typical signal delivered by the array of PMTs. Features as time separation between S1 and S2 and time extension of both signals are represented.

higher density of ionized and excited molecules. The extraction is higher for γ-rays (or electrons) than for nuclear recoils because the density of ionized species is lower, making the extraction operated by the electric field more effective. In this sense, the ratio of primary to secondary scintillation for nuclear and electronic recoils will be very different, providing the detector with discrimination capability (figure 2.5).

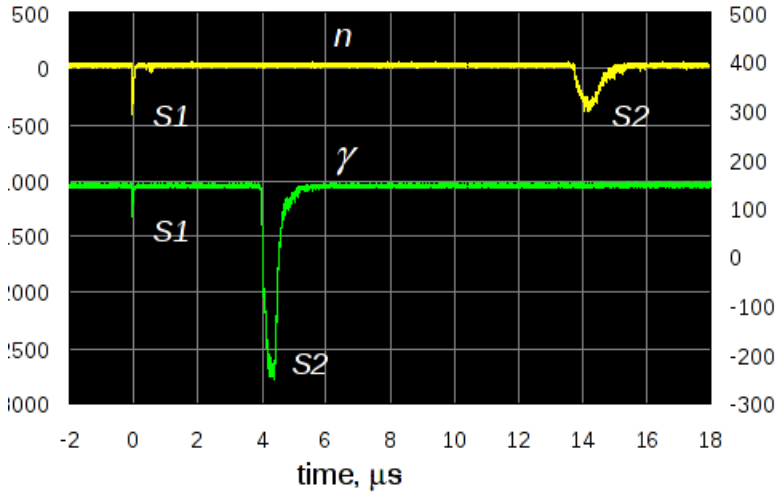

Figure 2.5: Example of two signals in ZEPLIN III, after a xenon recoil. The upper trace corresponds to the scattering of a neutron and the lower one to a γ-ray. *Image credit: ZEPLIN Collaboration.*

2.3.3 Other interesting features

ZEPLIN-III was made to detect rare events, which makes noise reduction major priority. This is achieved using high-purity, low-background components and by choosing an underground location to operate. The light collection is enhanced by immersion of the PMT array (QE is around 30% for each PMT) in the liquid. This maximizes the number of electrons collected, which is important, given the low number of photoelectrons expectable from a WIMP interaction. Light collection is also optimized by the thin geometry of the liquid volume, which diminishes

self-absorption effects.
To distinguish between nuclear and electronic recoils, it is necessary to have very uniform responses in both channels. This is achieved by limiting the active volume of the detector (fiducialization), which is possible by reconstructing the interaction position in order to reject events occurring beyond the limit for which light collection and electric field are no longer uniforms. Fiducialization has also the advantage of self-shielding: as liquid xenon is relatively dense, the peripheral layer acts as another shield protecting from background, in addition to the lead castle and active veto.

2.3.4 Position Reconstruction

As suggested in the previous section, position reconstruction allows fiducialization of the active volume. One advantage of this, is the possibility of excluding peripheral interactions that can be due to residual radioactivity of the detector walls. The other advantage is related with the field uniformity, as already stated. Particle interactions in the frontiers, where the electric field has non-uniformities can be identified and excluded.

The radial coordinates (x,y) can be reconstructed using a simple centroid method. Each coordinate is computed as the weighted mean of the coordinates signalized by each PMT (x_i), being the weigh delivered by each signal amplitude (A_i):

$$x = \frac{\sum_i x_i A_i}{\sum_i A_i}$$

and similarly for the y coordinate. This algorithm, using either the S1 or S2 signals, provides low position resolution. A more advanced algorithm, uses a least-square calculation. The response to a signal emitted in each (x,y,z) position is known and compared to the measured signal, being the position chosen according to the best agreement.
The depth of the interactions (z) is obtained from the time difference between the S1 and S2 signals (d_{time}), using the drift velocity (v_{drift}) of electrons in liquid xenon:

$$z = d_{time} \times v_{drift}$$

2.3.5 Energy Reconstruction

In ZEPLIN III, as in other similar dark matter detectors, the energy deposited by a WIMP is estimated using the primary scintillation signal, S1. Thus, it is a matter of crucial importance to know the scintillation yield of liquid xenon for nuclear recoils as a function of their energy. In practice, we are not actually interested in exact knowledge of the absolute light yield, but rather in the relative efficiency for recoils with respect to that for electrons. It is a common practice to calibrate the detector response with $122keV$ γ-rays from ^{57}Co. Therefore, if one knew the ratio of the scintillation yield for nuclear recoils to that for 122 keV γ-rays as a function of the recoil energy, the recoil energy can be determined from the observed scintillation signal and the calibration data. This ratio is usually called $\mathcal{L}_{eff}$:

$$\mathcal{L}_{eff}\left(E_R\right) = \frac{Y_R\left(E_R\right)}{Y_{122}}$$

The existing results on measurements of the relative scintillation efficiency, $\mathcal{L}_{eff}$, are presented in figure 2.6. The usual way to measure $\mathcal{L}_{eff}$ is to use elastic scattering of fast neutrons off a liquid xenon target with a dedicated chamber. This technique is described in [(23)] and [(24)].

$\mathcal{L}_{eff}$ is a function of the deposited energy and its behavior for low-energy recoils is not understood. We will study this issue in the following two chapters. Figure 2.6 shows the existing measurements of $\mathcal{L}_{eff}$ for three different scintillators, for a variety of impinging particles.

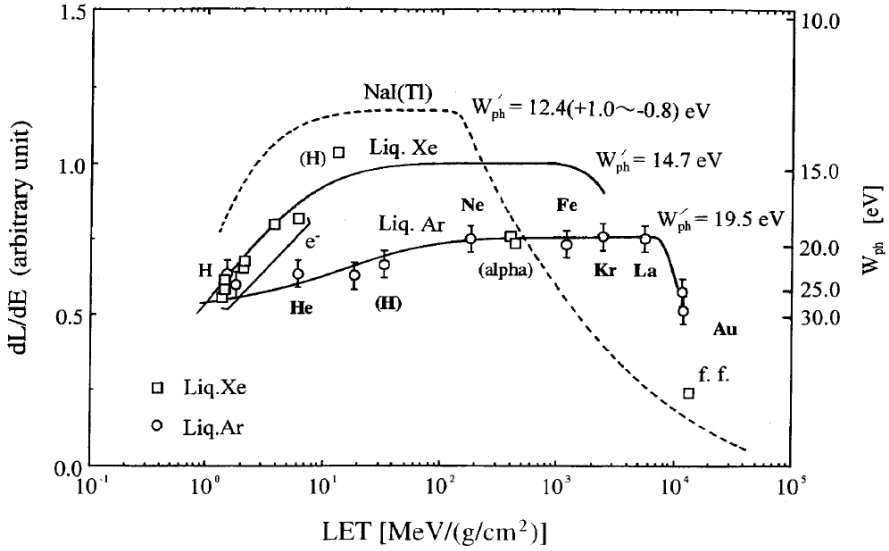

Figure 2.6: Scintillation yield for Xe, Ar and NaI(Tl) dependence on LET for a variety of impinging particles. W_{ph} represents the energy necessary to extract a photon from the atomic medium. Extracted from [(1)]

Chapter 3

Quenching of Scintillation light for Nuclear Recoils

The two-phase technique requires detection of both charge (ionization) and light (scintillation) produced along the particle track. These processes depend on the kind of particle and differ significantly for electrons and nuclear recoils. In the low energy region, which is of interest for the WIMP detection, not all the details are understood even in the case of electrons and γ-rays. Much less is known about scintillation and ionization due to low energy nuclear recoils. We shall consider some of the aspects of this important problem in this and the next chapters.

Scintillation efficiency of liquid xenon for low-energy nuclear recoils is crucial for ZEPLIN III or other noble liquid detectors searching for WIMPs. A problem these experiments find is the reduced (and not well known) scintillation efficiency when compared to electronic recoils. The cause for this is generally attributed to two mechanisms: *energy losses* through nuclear collisions and *scintillation quenching*. The main contribution is usually considered to be the energy loss in nuclear stopping that does not lead to ionization neither scintillation. This is described by Lindhard theory [(25)] and we will refer it as *nuclear quenching*. The other part, the scintillation quenching, can also be significant and is described by Birks saturation law [(26)]. It results from the nonlinear response of a scintillator to particles with different ionization density. As only the electronic stopping is

responsible for scintillation, the scintillation reduction will be identified as the *electronic quenching* from now on.

Electrons lose their energy interacting with atomic electron clouds of the detector media, promoting ionizations and/or excitations. In contrast, a recoiling nucleus will lose its energy in collision with electrons and with other nuclei. In this sense, the total stopping power can be found to be the sum of these two contributions:

$$\left(\frac{dE}{dx}\right)_{tot} = \left(\frac{dE}{dx}\right)_{e} + \left(\frac{dE}{dx}\right)_{n} \tag{3.1}$$

where the first term denotes the amount of energy per unit distance that the recoiling nucleus loses due to electronic excitation and ionization of the surrounding xenon atoms and the second term, the nuclear stopping power, is the energy loss per unit length due to atomic collisions that contribute to the kinetic energy of xenon atoms - thermal motion - without internal excitation of atoms. The proportion of electronic to nuclear stopping power depends on the energy of the impinging nucleus. For high energy recoils, the electronic stopping power would be several orders of magnitude larger than the nuclear one. But in the energy range of WIMP-nucleus elastic scatterings (chapter 2), the nuclear stopping power plays very significant role.

3.1 Lindhard theory of Energy Loss

Lindhard's theory describes the energy loss in nuclear stopping that does not lead to ionization neither scintillation. Choosing a non-dimensional energy variable

$$\epsilon = \frac{11.5}{Z^{1/3}} E_R$$

to represent the kinetic energy (E_R) of an ion[1] penetrating a medium with atoms of the same specie (Z). Supposing that the particle will lose all its energy (E_R) in the detector medium, we can divide this energy loss in two terms (similarly to

[1] the initial charge of the ion is not relevant, as it will change quickly according to the ions velocity, atomic number and surrounding media.

equation 3.1): the electronic stopping power η and the nuclear stopping power ν, being both function of the recoil energy ϵ:

$$\epsilon = \eta(\epsilon) + \nu(\epsilon)$$

The electronic energy loss is found to be $\eta = \kappa\sqrt{\epsilon}$, with $\kappa = 0.133Z^{2/3}A^{-1/2}$. The nuclear losses, in their turn, can be described by [(25)]:

$$\nu = \frac{\epsilon}{1 + \kappa g\left(\epsilon\right)} \tag{3.2}$$

where $g\left(\epsilon\right)$ is well fitted by $g\left(\epsilon\right) = 3\epsilon^{0.15} + 0.7\epsilon^{0.6} + \epsilon$.

The reduction factor due to nuclear losses can then be defined as:

$$q_n = \frac{\eta}{\epsilon} = \frac{\epsilon - \nu}{\epsilon} \tag{3.3}$$

Using equation (3.2),

$$q_n = \frac{\left(1 + \kappa g\left(\epsilon\right)\right)\epsilon - \epsilon}{\epsilon\left(1 + \kappa g\left(\epsilon\right)\right)} = \frac{\kappa g\left(\epsilon\right)}{1 + \kappa g\left(\epsilon\right)} \tag{3.4}$$

, giving the quenching factor due to nuclear losses as a function of the nuclear recoil energy. Figure 3.1 shows this calculation for xenon and argon.

Lindhard theory works well for semiconductors because, there, the scintillation arising from electronic stopping is unquenched. In most scintillators this is not the case.

3.2 Electronic Quenching

3.2.1 Dependence of Scintillation Yield on LET

In 1988, Doke et al. summarized a number of experiments that measured the Linear Energy Transfer (LET) dependence of scintillation yields in liquid argon for a variety of particles, which is included in figure 2.6. The light yield has been found to reach its maximum in the LET region of 10^2 to $10^3 MeVcm^2/g$, corresponding to the relativistic ions. This behavior was called by the authors "the flat-top response" and it was assumed that in this region all excited species created by a particle in the liquid emit a photon (i.e. there is no quenching).

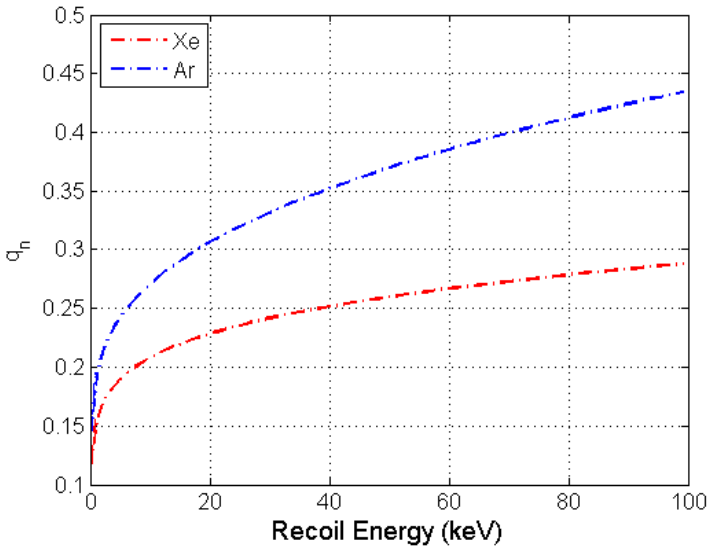

Figure 3.1: Fraction of the electronic losses of argon and xenon ions in the respective liquid.

In the other hand, the two sides of the plot are affected by quenching effects, which diminish the scintillation efficiency. For the low dE/dx, the effect results from the low density of ionized species, which makes recombination less probable. In the high dE/dx region, the effect is suggested to result from the high density of excited species, being biexcitonic[1] quenching a proposed mechanism. As a result of this process, from each pair of excited atoms will only result one photon. Birks saturation law is a phenomenological equation which relates scintillation reduction with these processes.

3.2.2 Birks Saturation Law

The track of particle passing through a noble liquid medium is conveniently described in terms of a core and a penumbra. The core consists on a high excitation density region, produced by the primary particle interaction and, to some extent, some δ-electrons. The penumbra is the surrounding volume, where δ-electrons

[1] When studying Hitachi's treatment, we will see how this process works for xenon scintillators.

are responsible for the existing lower excitation density. Biexcitonic collisions and the Penning process are quenching processes, acting on the excitons produced along the track. The number of excitons and electron-ion pairs produced along the track is proportional to the electronic energy loss ($(dE/dx)_{elec}$), and we will denote the proportionality constant as A. The local concentration of the core is also proportional to the ionization density (B is the proportionality constant). So, Birk's saturation law gives the relative scintillation response of scintillators to an ionizing particle of any energy as [(26)]:

$$\frac{dS}{dx} = \frac{A\frac{dE}{dx}}{1 + kB\frac{dE}{dx}}$$

where k is the overall collision probability in the core. Both factors A and kB are to be determined experimentally. According to this equation, the scintillation yield is reduced at high ionization densities. We can define a quenching factor:

$$q_{el} = \frac{1}{1 + kB\frac{dE}{dx}} \tag{3.5}$$

For liquid xenon, and according to [(23)], for 70 keV recoil, Birks constant κB is $2.015 \times 10^{-3} MeV^{-1} gcm^{-2}$. For liquid argon, $\kappa B = 7.4 \times 10^{-4} MeV^{-1} gcm^{-2}$ [(27)].

Birks law is a phenomenological equation which has shown considerable successes in explaining the LET dependence of scintillation yields for organic scintillators, where the scintillation and quenching mechanisms are presumably complicated. Still, it fails to explain the scintillation efficiency reduction in condensed noble gases. As we will see now, this is better achieved by Hitachi's treatment.

3.2.3 Hitachi's Treatment

Hitachi treatment tries to explain the reduction of the overall scintillation efficiency in liquefied noble gases using Lindhard's theory to correctly describe nuclear quenching and presenting a mechanism for the electronic quenching that, like in Birk's theory, includes biexcitonic collisions. In xenon, the scintillation

is delivered by the eximers Xe_2^*, which are created from free excitons Xe^*. In biexcitonic collisions, two of these excited states meet:

$$Xe^* + Xe^* \rightarrow Xe + Xe^+ + e^-(K.E.)$$

The electron then carries away and loses energy close to an excitation energy before recombining. In this process, only one photon is produced by the pair of excitons, when two could be expected.

This makes the description of the track structure and energy migration within the detector features of major importance. The quenching factor will not only be a function of LET, but it will also be related to the quality of the ionizing particle. Like in Birks theory, we can consider the heavy-ion track as being composed by a core and a penumbra. Quenching is assumed to take place only in the high excitation density core.

So, as a final result, the total quenching will be the product of nuclear and electronic quenchings described by equations 3.4 and 3.5:

$$Q = q_n \times q_{el}$$

This is the best prescription for the understanding of the total scintillation efficiency reduction in liquid noble gases.

Chapter 4

Simulation of the Interaction of Low-Energy Ions with Matter

As discussed in Chapter 3, the process through which a low-energy heavy ion will lose its energy in a detector is not easily described. We will now explore how simulation toolkits like SRIM and GEANT4 deal with them and how do they compare with the scarce existing measurements.

As a result of inquiries during the workmanship of this thesis, I have traded a few emails with Dr. James F. Ziegler. Through this contact, Dr. Ziegler has kindly handed over a collection of Scientific Citations of Experimental Data of measurements concerning low-energy Xenon ions. This list is not available in SRIM's website[1] where the other citations are to be found. In the interest of the reader, I have stored them in Appendix 1.

4.1 GEANT4

GEANT4 is a toolkit for the simulation of the passage of particles through matter. It is an ever evolving public code, whose performance is enhanced every year. In the context of this chapter, particular interest is devoted to the nuclear stopping power. Moreover, this will be a validity test to a class introduced in 2005 that

[1] http://www.srim.org/

lacks verification: the G4ScreenedNuclearCoulomb [(28)]. This class is the only one available that allows to follow nuclear recoils produced by an incoming particle. As for the electronic stopping power, we rely on the class G4IonIonization. This class could also provide nuclear stopping, but the flag for this feature will be turned off, as it only makes local depositions of energy without the creation of a recoiling nucleus. A short description of both classes and methods is found in the following introductory sections.

4.1.1 Electronic Stopping - G4IonIonization

G4IonIonization manages the ionization process for ions. Effective charge, nuclear stopping power and energy loss corrections can be taken into account. It has been recently added (June 2009) as a replacement for classes like the G4ionLowEnergyIonization, for the simulation of ions energy loss. The ion parameterized energy loss model, through which the stopping power is computed, adopts the following rules:

A. If the ion-material pair is covered by any native ion data parameterization, then:

- This parameterization is used for energies below a given energy limit,
- above the limit the Bethe-Bloch model is applied, in combination with an effective charge estimate and high order correction terms. A smoothing procedure is applied to dE/dx values computed with the second approach. The smoothing factor is based on the dE/dx values of both approaches at the transition energy (high order correction terms are included in the calculation of the transition factor).

B. If the particle is a generic ion, the "BraggIon" (described in the following paragraphs) and Bethe-Bloch models are used and a smoothing procedure is applied to values obtained with the second approach.

C. If the ion-material is not covered by any ion data parameterization then:

- The "BraggIon" model is used for energies below a given energy limit,

- whereas above the limit the Bethe-Bloch model is applied, in combination with an effective charge estimate and high order correction terms. Also in this case, a smoothing procedure is applied to dE/dx values computed with the second model.

4.1.1.1 Models and Parametrizations

The class G4IonIonization provides, not only the continuous energy loss due to ionization, but also the "discrete" production of $\delta-$rays. As stated, it can use three models: the Bethe-Bloch model (for protons with energy greater than 2 MeV); the G4BraggModel (for protons bellow 2 MeV) and the G4BraggIonModel for heavier ions of any energy. In all these cases, the maximum energy transferable to a free electron (mass m_e) from an incoming particle (with mass M) is given by [(29)]:

$$E_{max} = \frac{2m_e c^2 \left(\gamma^2 - 1\right)}{1 + 2\gamma \left(m_e/M\right) + \left(m_e/M\right)^2}$$

where γ is the Lorentz factor. In the scope of this chapter, our interest concerns the G4BraggIonModel. Further looking into this class, one will find that parametrization of evaluated data for stopping powers at low energies is used. This parametrization is available for all atoms from the ICRU'49 report [(30)]. Data from the NIST databases for specific materials are also included but they are out of our interest, since we will be looking into simple symmetrical combinations of argon(xenon) ions arriving at argon(xenon) targets for which ICRU'49 suffices.

An important topic to consider is the charge of the ionizing ion. As the ion travels through the medium, it exchanges electrons with other atoms. G4ionIonisation calculates the effective charge of the ion according to its kinetic energy in a given material. Before and after each step, the effective charge (z_{eff}) is computed from the charge of the stripped atom (z_i):

$$z_{eff} = \gamma_i z_i$$

where γ_i is a function of the ion energy described in Appendix C. This effective charge parametrization is to be applied if the kinetic energy is below a limit value:

$$E_{lim} = 10 z_i \frac{M_i}{m_p} (MeV)$$

where M_i is the ion mass and m_p is the proton mass. So, in our low-energy regime, it will always be applied.

4.1.2 Nuclear Stopping - G4ScreenedNuclearRecoil

Nuclear stopping power can be added to the energy loss, when using the process G4ionIonization. This class has a flag which allows to switch on or off this contribution. By default, this correction is active and uses the ICRU'49 parametrization [(30)]. This feature will only introduce local energy deposits along the primary particle track. In this work, we will disregard nuclear stopping provided by G4ionIonization class and use a new physical process, the G4ScreenedNuclearRecoil to describe nuclear stopping in a more realistic way, by the implementation of nuclear recoiling secondaries. This class is described in reference [refscreen]. It has been recently introduced and, as stated by its authors, still lacks validation as it was only tested in an intermediate energy range. This work is an opportunity to assess its results in the low-energy regime, while comparing it with other code (TRIM) and with some experimental results.
The scattering is assumed to be classical, with the interactomic potential described by the potential

$$V(r) = \frac{Z_1 Z_2 e^2}{r} \phi \left(\frac{r}{a} \right)$$

where Z_1 and Z_2 are the nuclear proton numbers of incoming ion and stationary target, e^2 is the electromagnetic coupling constant (equal to $q_e^2/4\pi\epsilon_0$ in SI units) and r is the inter-nuclear distance. ϕ is a reduction factor due to electronic screening of the bare nuclear charges. Is is known as the screening function and is a function of the inter-nuclear distance and a characteristic length scale for the screening, a. There are several models for this screening function. Figure 4.1 resumes available proposals. Further details are provided in Appendix B.

The screening reduction are very close to each other, for small inter-nuclear distances. As distance between intervening ions grows, distinction among them

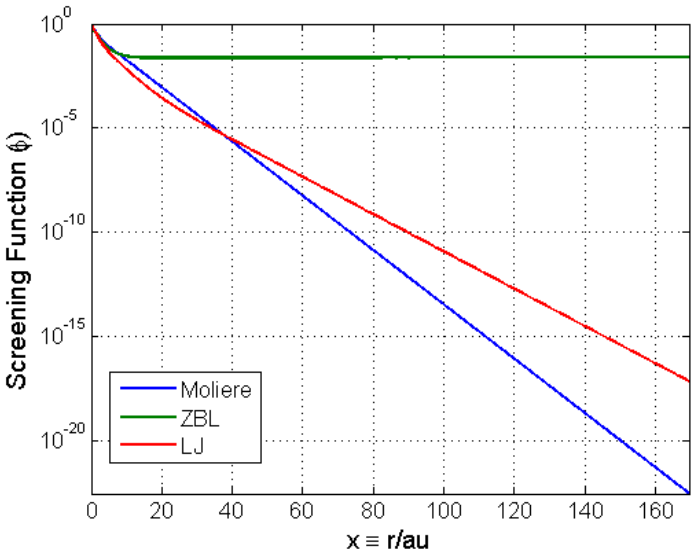

Figure 4.1: Nuclear screening functions.

is enhanced. This region, of bigger separation is the most important for the slow-heavy ion case, since the low kinetic energy will not allow great penetration in the Coulomb fields.

4.1.3 Validation

4.1.3.1 α-particle in Water

As a first test to the simulation, a light ion of intermediate energy is studied. The Bragg curve of a 5.49 MeV α-particle (from ^{222}Rn source) in water is shown in Figure 4.2, where GEANT4 result is compared to the TRIM corresponding.

Good agreement between both codes is found. The authors of the class G4ScreenedNuclearRecoil also found good agreement for the range of alpha-particles in air, for a wide range of energies. We will now see if the agreement remains for heavier ions.

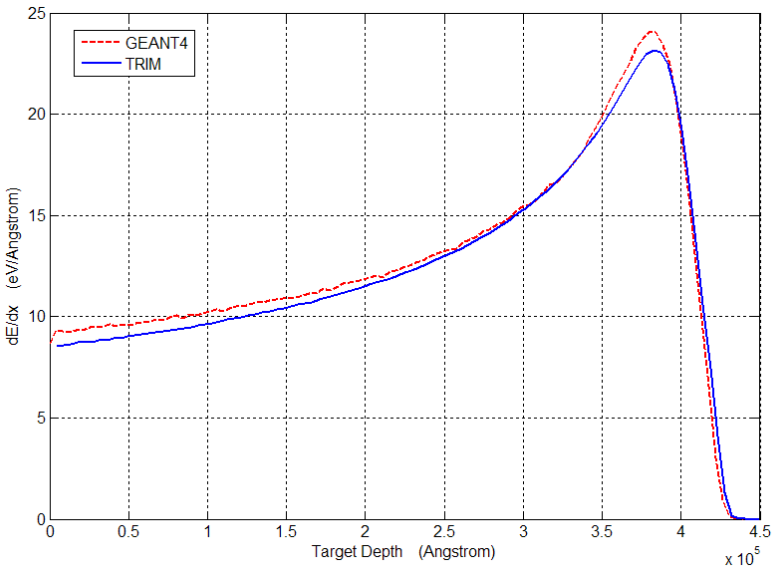

Figure 4.2: Bragg curve for 5.49 MeV alpha-particle in water.

4.1.3.2 Xenon Ion in Liquid Xenon volume

Figure 4.3 shows the range of xenon ions in xenon with density equal to 3.0589 gcm^{-3} corresponding to the density of liquid xenon at triple point. The *Recoil-Cutoff*, which is the energy below which no new moving particles will be created, is set to the xenon atoms binding energy in the lattice: 1 keV (according to TRIM). All these conditions are the same for both TRIM and GEANT4. Figure 4.3 shows comparison of the results.

4.1.3.3 Argon Ion in Liquid Argon volume

Argon is also a detection medium of interest for dark matter experiments. Figure 4.4 shows comparison of TRIM and GEANT4 range calculation.

4.2 Scintillation Efficiency Estimations

Chapter 3 has resumed the theory about scintillation efficiency reduction. We are particularly interested in the effects concerning liquefied noble gas detectors,

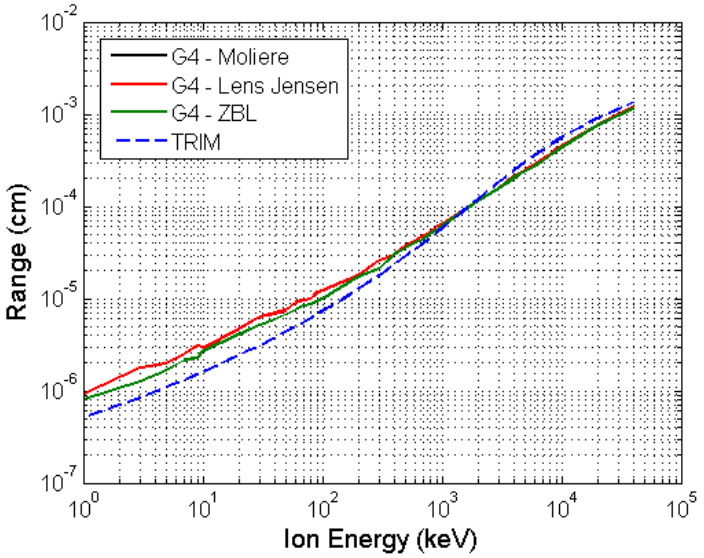

Figure 4.3: Xenon range in a liquid xenon target.

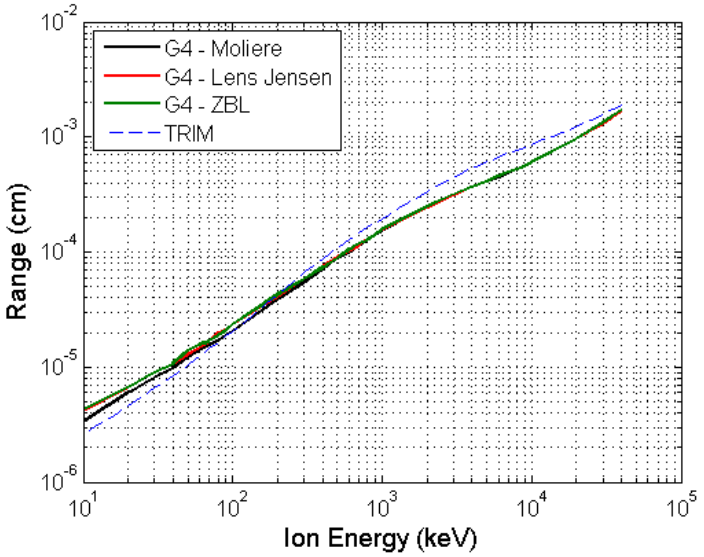

Figure 4.4: Argon range in liquid argon target.

which are most successfully described when considering a quenching of the scintillation according to

$$Q = q_n \times q_{el} \tag{4.1}$$

, where both nuclear and electronic quenching contributions are taken into account. With the simulation tool we have been studying through this chapter in mind, one can naturally ask what does the simulation predict for the $\mathcal{L}_{eff}$ of interesting combinations of ions and targets, and how does this prediction compare with existing measurements.

What we will be able to obtain from GEANT4 will be the total quenching factor for the recoiling ion, $Q(E_R)$. The G4ScreenedNuclearRecoil was developed by a group interested in semiconductors damage and doping by incoming ions, who are very interested in the Non Ionizing Energy Loss (NIEL) in such processes. For each ion of a given energy (followed till it comes to rest), this is the energy transfered to displace atoms from their original position and move them though the lattice (we will identify this as E_{NIEL}). The nuclear quenching for a given ion energy will then be

$$q_n = \frac{E_R - E_{NIEL}}{E_R}$$

so that $q_n = 1$ if no energy is delivered to atomic motion. As for electronic quenching, it is calculated from Birks saturation law (equation 3.5), where the constants kB are found in the literature (see section 3.2.2) and the corresponding dE/dx for each combination is calculated from the simulation's first step length and respective energy deposit.

The scintillation efficiency ($\mathcal{L}_{eff}$) for the recoiling ion will then be the ration of its light yield ($Y_R(E_R)$) to that corresponding to a 122 keV electron ($Y_e(122keV)$):

$$\mathcal{L}_{eff} = \frac{Y_R(E_R)}{Y_e(122keV)} \tag{4.2}$$

Of course, both these light yields are reduced from the maximum flat top by a given quenching factor:

$$Y_R\left(E_R\right) = Y_{max} Q\left(E_R\right) \tag{4.3}$$

and

$$Y_e\left(122keV\right) = Y_{max} Q\left(122keV\right) \tag{4.4}$$

Introducing expressions 4.3 and 4.4 in equation 4.2, leads to

$$\mathcal{L}_{eff} = \frac{Q\left(E_R\right)}{Q\left(122keV\right)} \tag{4.5}$$

In the following, $\mathcal{L}_{eff}$ computations for xenon and argon from the GEANT4 simulation are presented, where the quenching factor $Q\left(E_R\right)$ is obtained from the dynamical consideration within the simulation and the quenching for 122 keV electrons in both targets is extracted from the literature. This, is found to be ∼0.75 for liquid xenon and ∼0.8 for liquid argon, using $\mathcal{L}_{eff}$ measurements from figure 2.6.

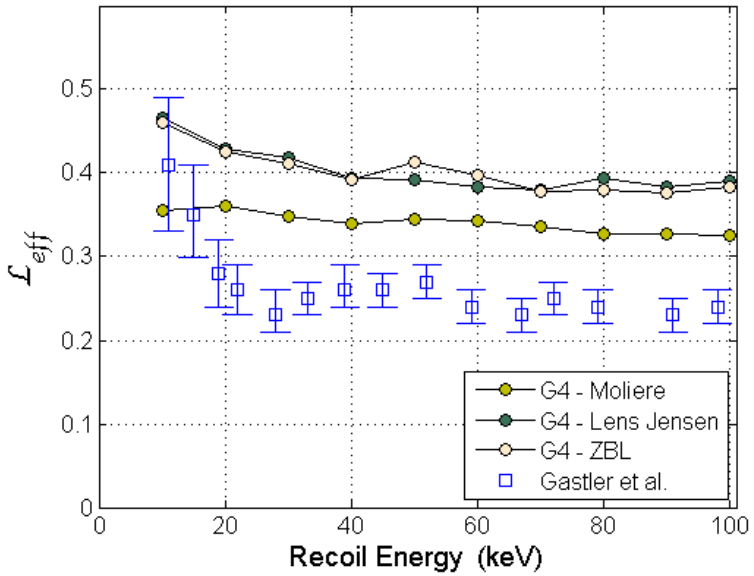

Figure 4.5: Argon $\mathcal{L}_{eff}$ as simulated by GEANT4 and compared to existing measurements.

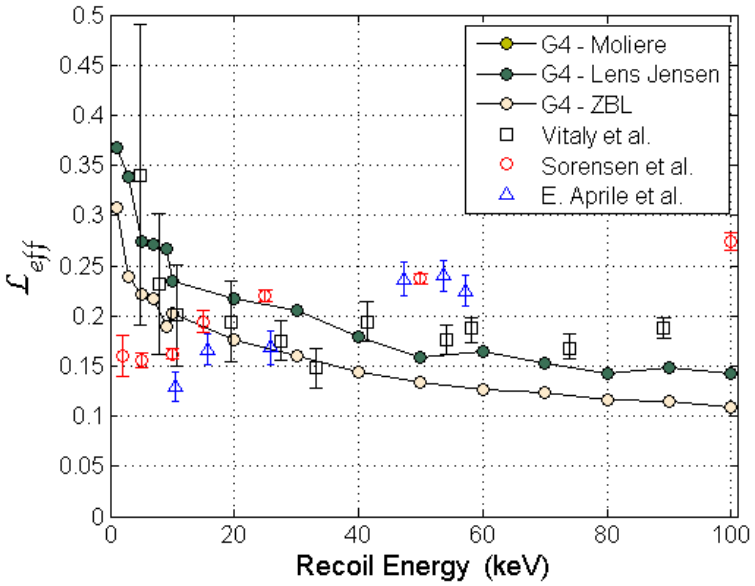

Figure 4.6: Xenon $\mathcal{L}_{eff}$ as simulated by GEANT4 and compared to existing measurements.

The result obtained, in particular for xenon, is very close to experimental measurements in the region above 20 keV. Approaching lower energies, where experiments show different tendencies, the simulation agrees with those suggesting an up going curve.

Chapter 5

The Single Electron Signal

In this Chapter we will explore a particular signal arising in the ZEPLIN III detector: the Single Electron (SE) signal, which is the detector response to the extraction of a single electron from the liquid phase. In the following discussion, two different arguments are presented concerning the utility and relevance of this particular signal.

As said in Chapter 2, energy reconstruction in two-phase noble detectors (like ZEPLIN III) is done using the primary scintillation signal (which is called S1). The secondary scintillation signal (S2) is only used as a discrimination factor. However, it has remarkable sensibility and could be used to provide another calculation of the energy deposited by the recoiling particle, if the charge extraction efficiency is known. This would be advantageous for detectors searching for rare, weak signals because it would lower the energy threshold. In ZEPLIN and dark matter detectors particular case, this argument loses its significance, as the energy threshold of the detector is dictated by the less sensitive S1 channel: there is no point in reconstructing the energy of an interaction bellow this point, if we are to lose the discrimination capability of the detector, which requests the ratio of both signals.

While a detector capable of measuring single electron signals can benefit from the low-energy threshold described in the last paragraph, it can also be affected by an unwanted noise feature, as we found in ZEPLIN III. The origin of these

noisy events is explored in section 5.4. These spurious signals do not disturb ZEPLIN III results, since they do not provide a WIMP-like signature.

5.1 Signal Estimation

The SE signal is created when, for some reason, a electron is made free in the liquid and drifts into the gas, due to the applied high voltage. As explained in section 2, the strong electric field in the gas, just below the multiplication limit, accelerates the electron before it interacts with a xenon atom. If the electron has gained enough kinetic energy, it can excite the xenon atom, which de-excites producing a 175 nm VUV photon. Otherwise the energy is lost. This produces a field and pressure dependence on the signal. The process is repeated until the electron leaves the electric field. An estimation of the number of photons emitted can be made, using the formula

$$N_{ph} = ax\frac{E}{n} + bx$$

, where E represents the electric field, $n = N_A\rho/A$ is the density of atoms calculated from the saturated vapor density (ρ), and $x = nd$ is the number f atoms per unit area through the electroluminescence depth d. For xenon saturated vapor at cryogenic temperatures, reference [(31)] suggests $a = 0.137\,V^{-1}$ and $b = -4.7 \times 10^{-18}\,cm^2/atom$. All together, the formula predicts 300 photons will be emitted as an electron drifts across the gas gap. The VUV photons then travel around the detector undergoing reflections and refraction with a fraction of them impinging the array of PMT photocathodes. This light collection efficiency was predicted by a Monte Carlo study [(32)]. For events in the center, it is about 38%. Quantum efficiency estimates the fraction of photons which produce photoelectron emission at their arrival to the photocatode, generating a signal in the PMTs. For the central 17 PMTs, the average quantum efficiency is about 32%. These numbers suggest that an electron emitted into the gas phase in the central region of the detector would produce a signal of about 36 photoelectron in the PMT array. Figure 5.1 shows typical SE signals found in ZEPLIN III.

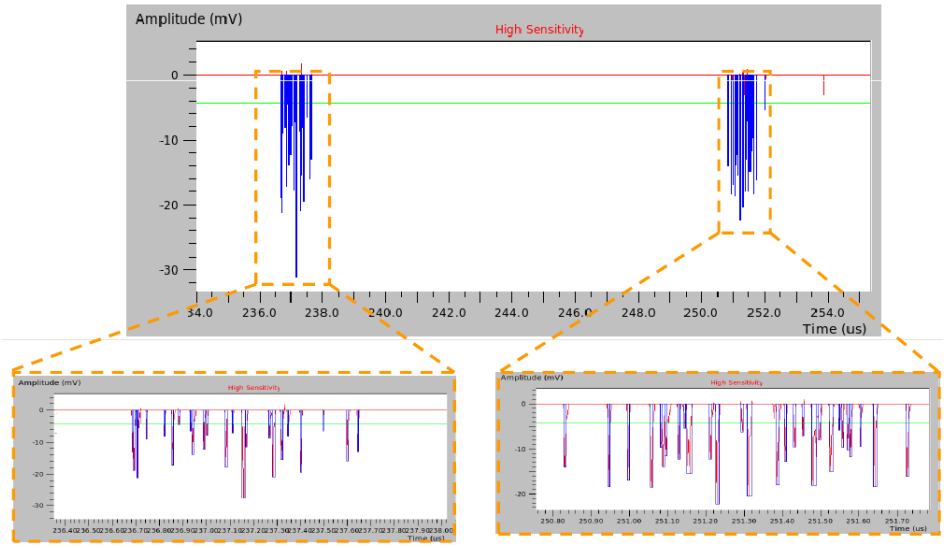

Figure 5.1: Waveform with two single electron clusters. In the zoom, one can see the individual photo-electron pulses that build the signal.

5.2 The SE dedicated run

5.2.1 Description

The dedicated SE data set was acquired with the DAQ triggering from an external pulser (100 Hz). The PMT signals were digitized at 2 ns sampling over a time segment of 256 μs starting at the trigger instant. A total of 163 s were acquired during two days, immediately after the First (dark matter searching) Science Run and calibration with ^{57}Co and $Am - Be$ sources. Software trigger at the single photoelectron spectrum valley. The pressure in the liquid chamber during the run was 1.6 bar. The raw data were reduced using a software threshold of $V_{thr} = 6\sigma$. The event selection was made using a routine that looked up for at least 3-fold coincidence in 1 us time-window (which is about 20% longer than the time required for an electron to cross the gas gap). Two selection cuts are further applied:

- the previous 20 us in the timeline are required to be clean of events. This is the time an electron takes to drift across the whole liquid depth. This

cut tries to ensure that the single electron events we found are not due to a photoionization process from a previous event in the LXe (at least, in a direct manner). The surviving events are labeled "*quiet*" events.

- only the volume corresponding to the inner 60 mm radius is used, since noise dominates the signals provided by the outward regions. This is the *fiducial* selection.

The population of events which survive both cuts will be labeled "*selected data*".

5.2.2 Results

The number of photoelectron pulses in the SE cluster is found using two methods. One way is to simply count the number of times the signal arises above threshold (Figure 5.2). This counting process may be affected by peak coincidences.

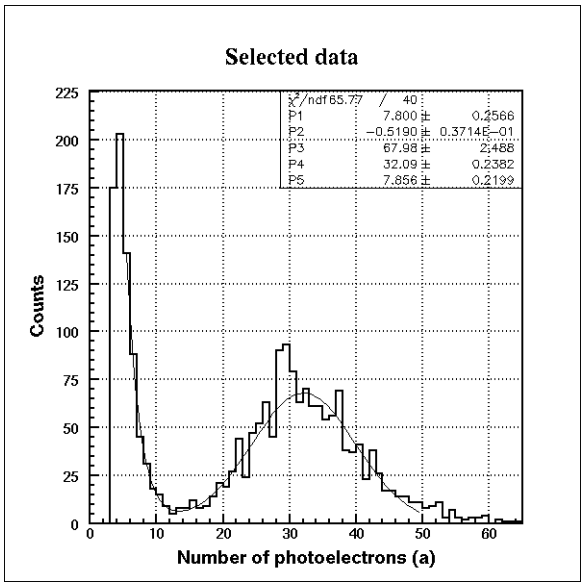

Figure 5.2: Number of photoelectrons in the Single Electron signal, using individual peak counting.

The other process uses the pulse integrated area, which, divided by the mean

area of the single photoelectron pulse in the respective PMT (independently measured), delivers the number of photoelectrons counted (Figure 5.3).

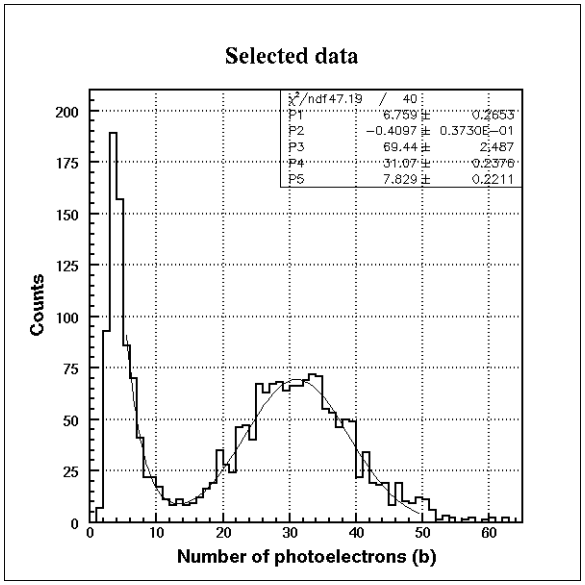

Figure 5.3: Number of photoelectrons in the Single Electron signal, using the area integration method.

Both distribution shows an exponential noise pedestal preceding the well separated SE peak, which is fitted with a Gaussian function. The mean is calculated to be $32.1 \pm 0.2/31.1 \pm 0.2$ with a distribution width of $\sigma = 7.9$ and 7.8 photoelectrons for pulse counting and area integration methods, respectively. The Poisson statistics would suggest a lower $\sigma \approx 5.6$, thus indicating existence of other sources of fluctuations. Good agreement is found between both methods (pulse counting and area integration) and for now on, we will always use the area integration method to obtain the total number of photoelectrons in the clusters.

Position reconstruction is possible in the xy plane (Figure 5.4). A simple centroid algorithm was implemented, showing uniform production of signals through the whole plane. Exception is made for events shown above PMTs number 23 (noisy) and 31 (switched off). In the bulk, the number of counts per unit area is

rather uniform (Figure 5.5).

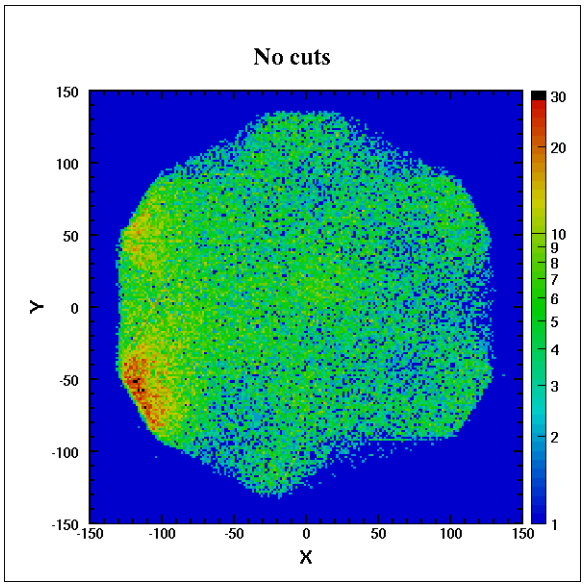

Figure 5.4: Radial coordinates of single electron events.

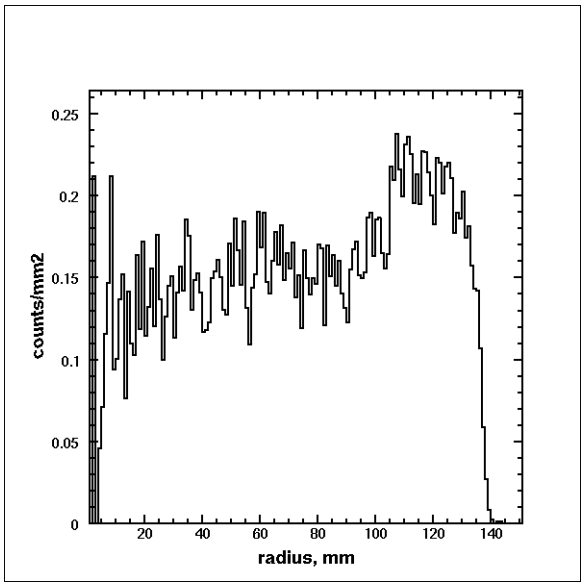

Figure 5.5: Radial distribution of single events though the detector.

The time extension of the single electron cluster can be computed from the gaseous depth the electron must cross and from the average speed of the electron in this volume, which is a function of the applied electric field and vapor pressure. This time is expected to be approximately 800 ns. Figure 5.6 shows the measured cluster durations.

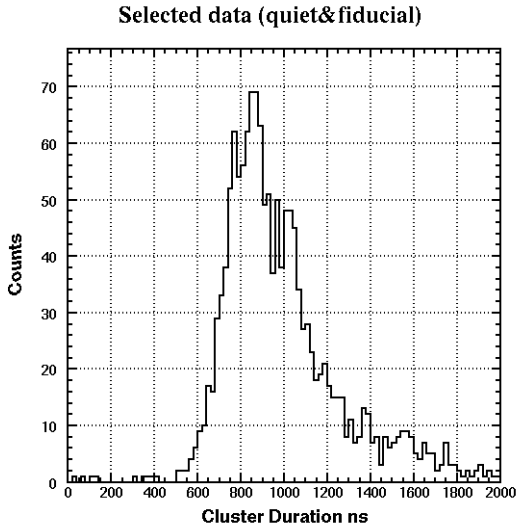

Figure 5.6: Duration of the single electron signal.

Although the peak centers in the expected value, there is a right-tail which is not understood. One possible mechanism providing time extension of the cluster could be the signal overlap of two electrons arriving at the gas phase in a short time interval. But this possibility is disregarded, as there is no corresponding two-electron peak with a mean of 62 photoelectrons in Figure 5.3.

The variation of the cluster duration along the detector radius was investigated. This is shown in figure 5.7.

The abnormal long-duration events are found to be produced uniformly through the detector radius.

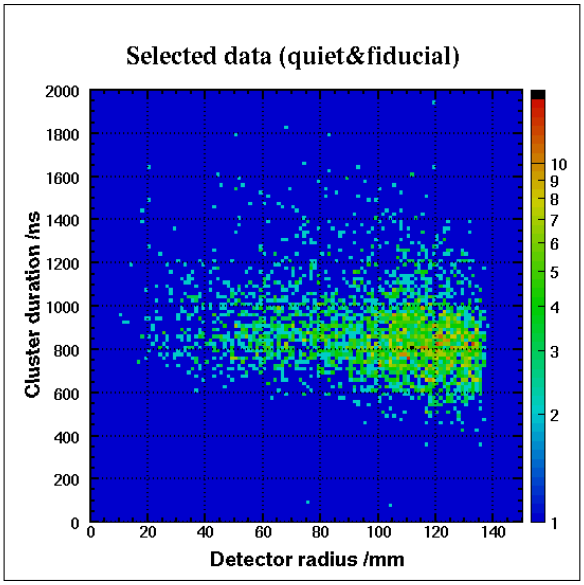

Figure 5.7: Variation of the cluster duration along the detector radius.

Other dependencies were studied. In these, separation of the SE peak events from those in the noise pedestal is typically found. For instants, in figure 5.8 is shown the variation of the number of photoelectrons in the cluster along the radius of the detector and in figure 5.9 is plotted the distribution of cluster duration against the of photolectrons in the cluster.

A key information given by the dedicated SE run is the spontaneous SE event rate in ZEPLIN III. In the 163 s data set, 2190 events where found using the selection cuts, giving an event rate of $13.4\,Hz$ ($10\,Hz.kg^{-1}$). Without cuts, the total number of events found is 108941, which gives an event rate of $668.4\,Hz$ ($79.1\,Hz.kg^{-1}$).

This event rate is relatively high. In reference (33) a measurement of SE in liquid Xe found an event rate of $0.5 \times 10^2\,Hz \cdot kg^{-1}$ at ground-level and without shielding. The factor of fifty which relates the two measurements weights the contribution of radiation to the formation of the SE signal.

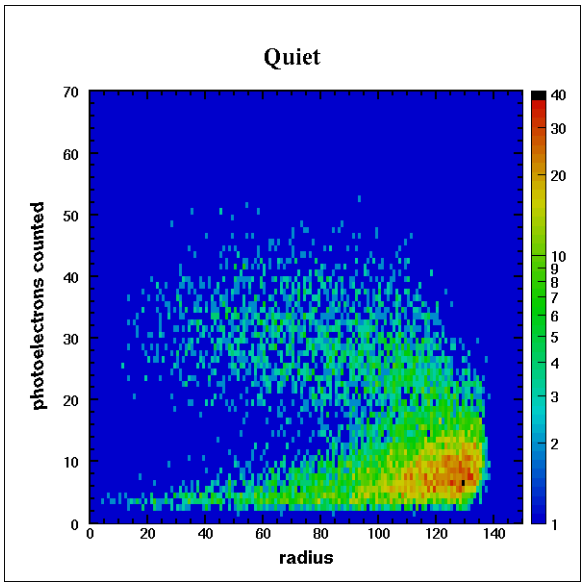

Figure 5.8: Clear separation between noise population (bottom, right) and SE peak-events (at the center).

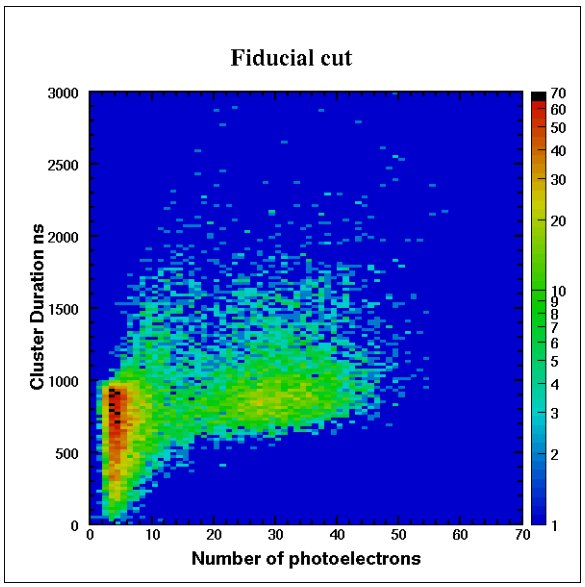

Figure 5.9: The cluster duration plotted against the number of photolectrons in the cluster also shows clear separation between noise and SE population

5.3 The First Science Run Contributions

The First Science Run (FSR) is a WIMP-searching data collection that gathered raw data during a total exposure of 847 kg.days. The run started on the 27th of February 2008 and lasted 83 days. The signals extracted from the 31 PMT array were collected through high and low sensitivity channels, delivering 62 waveforms. A population of small secondary signals was found after large secondaries and between S1 and S2 pulses. These were studied and provide an independent measurement of SE events in ZEPLIN III using a completely different data source and analysis.

Several results from the dedicated Single Electron run have been shown in the previous paragraphs. When compared with the FSR equivalents, good agreement is found. More concretely, the two independent analysis agree in the mean number of photoelectrons in ZEPLIN III single electron signal ($\sim$31).

Still, these data takings deliver signals that have different origins: while the SE run concerns the formation of spontaneous SE signals in the detector, allowing a measurement of this event rate, the FSR data set is related with photon-induced SE signals: i.e., the SE signal, which arrives a short-time interval after an S1, is likely to be related with the propagation of photons in the detector. Having a S1 component, this data set allows depth reconstruction (as described in section "*Position Reconstruction*"). Figure 5.10 shows a peak in the cathode grid position, suggesting electron extraction might be occurring there, by photo-electric effect.

5.4 Origins of the Signal

The origins of the SE signal in ZEPLIN-III were not clear before this work and were not clear for previous ZEPLIN-II either [(34)]. Possible emission mechanisms can be divided in two categories: photon induced and spontaneous. The former is associated with the FSR data set and the latter with the dedicated SE run (if we consider the probability of a spontaneous emission finding its place

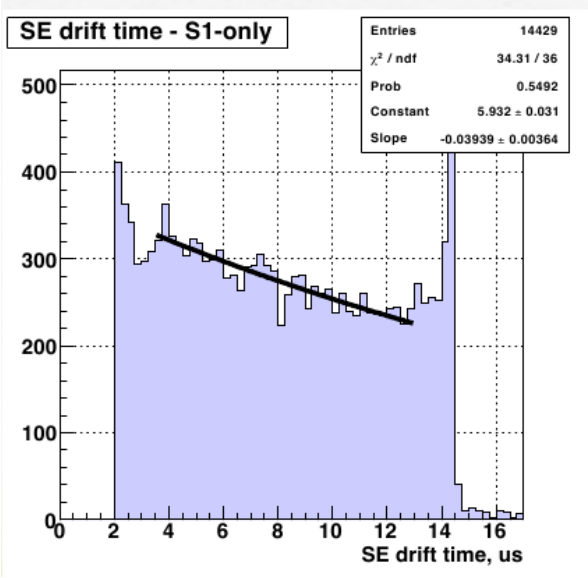

Figure 5.10: Depth of single electron events in the First Science Run.

between a S1 and a S2 negligible).

Photon induced emission can happen in the liquid Xe volume by photoionization of xenon or impurities. This is an effect we would expect from the beginning since the presence of electronegative impurities (typically, O_2, H_2O and N_2O) can be minimized, but not avoided. From the electron lifetime calculated above ($28.6\,\mu s$) and the attachment rate constant [(35)], the impurity concentration is found to be $3.6 \times 10^{15}\, atoms.cm^{-3}$. Comparing with the Xe concentration of $10^{22} cm^{-3}$, the relative concentration of impurities is 0.36 ppm. However, evidence of other production mechanisms is found. Depth reconstruction in the FSR data set shows uniform distribution through the liquid and a peak at the cathode grid position (figure 5.10). Electron emission can occur in the surface of cathode wires, due to photoelectric effect. In most metals, the quantum efficiency is not greater than 0.1%. Admitting a S2 formed along the middle of the gaseous phase, the "light collection efficiency" for the cathode grid will not be greater than 38% (which is the light collection efficiency for the PMT array right below it). Assuming as before that 300 photons will be emitted, an optimistic

calculation predicts that $300 \times 0.38 \times 0.1 \approx 11$ electrons will be extracted from the cathode grid. This is a crude estimation, better knowledge of the efficiency factors is required for a more accurate calculation.

As for spontaneous emission, we can consider the detachment of a previously captured electron from an electronegative impurity and field emission from the cathode wire. Here, the dedicated SE run can not rule out this latter surface effect (as depth reconstruction is not possible). Yet, in a crude estimation, we find that the electric field at the wire surface is $140kV/mm$, which is much lower than the lowest electric fields described in the existing literature on field emission (which are several MeV/mm). However, the energy level of a liquid Xe electron is lower than in vacuum or gas. We can't make a quantitative estimation of the event rate for this process (if any), but it does not seem significant. Another possible residual effect can be the emission from the liquid surface. This is possible because the extraction efficiency to the gaseous phase is not 100%. The electrons that remain in the liquid can be emitted to the gas at any moment.

5.5 Importance of the Single Electron signal

As stated before, capability of measuring single electron signals can be important for experiments searching for small, rare events, as it might allow to set a low threshold. In ZEPLIN III, this will not be the case for the dark matter runs (since the threshold is to be set by the primary scintillation signal - see discussion in the beginning of this chapter). Here, we explore a potential new application for the ZEPLIN III detector, motivated by the measurement of single electrons: the search for the never measured coherent neutrino-nucleus scattering.

5.5.1 Coherent Neutrino Scattering

Coherent neutrino scattering (CNS) from a nucleus is a predicted high rate interaction. Neutrinos interact with the nucleus in the same way as the hypothetical WIMP particle: via weak interactions. Though, as the neutrino is much lighter than the target atom, the energy transfer efficiency is much lower than in the WIMP case, making the expected signal much weaker. For a MeV neutrino, the

energy transferred to a Xe atom will be roughly ≈ *several* keV [(36)]. Few photons are emitted and few charge will be extracted. We cannot hope to measure the primary scintillation signal, as such a small number of photons (probably already to few to overcome the threshold) will not reach the PMTs due to light collection efficiency. However, even if the extracted charge is minimum (one electron), a measurable signal will be produced in ZEPLIN III.

A detector capable of measuring CNS could be used as a portable reactor monitor device. Existing neutrino detectors are very massive; CNS detectors proposed have only a few kilograms ([(37)]). Also, since the process is flavor blind (it involves a neutral current), any fluctuation on neutrino flux would be an indicator of sterile neutrino production.

5.5.1.1 The process

First proposed by Freedmann, 1977, CNS has never been measured. In this process, a neutrino of any flavor scatters elastically off a nucleus at low momentum transfer. This requirement is necessary so the wavefunction amplitudes are in phase and add coherently: the neutrino interacts with all nucleons at one time and the interaction cross section is proportional to N^2:

$$\sigma_{total} = \frac{G_F^2}{4\pi}\left[Z\left(4\sin^2\theta_W - 1\right) + N\right]^2 E_\nu^2 \approx \frac{G_F^2}{4\pi} N^2 E_\nu^2 \tag{5.1}$$

being G_F is the Fermi constant, Z the proton number of the target nucleus, N the neutron number, θ_W the Weinberg angle and E_ν the neutrino energy. (Note that using $sin\theta_W^2 = 0.23$ allowed to simplify the expression.) Despite $\sigma_{tot} \propto N^2$, it is not clear that heavier atoms make better targets, because for these, the energy transfer efficiency is lower. Both dependencies must be studied. Figures 5.11 to 5.13 show some calculations based on Hagmann's paper [(37)].

5.5.1.2 Rate Estimation

The scattering rate is given by

$$R = N_t \int_{E_{th}}^{\infty} dE_\nu \Phi\left(E_\nu\right) \int_0^{(E_{rec})_{Máx}} dE_{rec} \frac{d\sigma\left(E_\nu, E_{rec}\right)}{dE_{rec}} \tag{5.2}$$

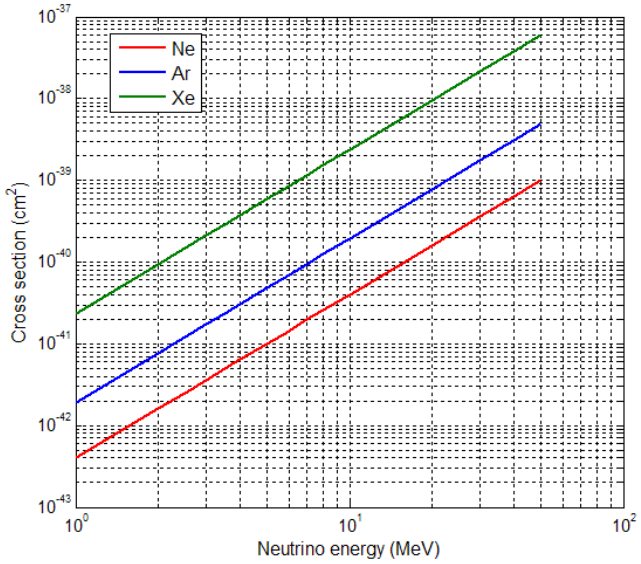

Figure 5.11: CNS cross-section for interaction with different target species.

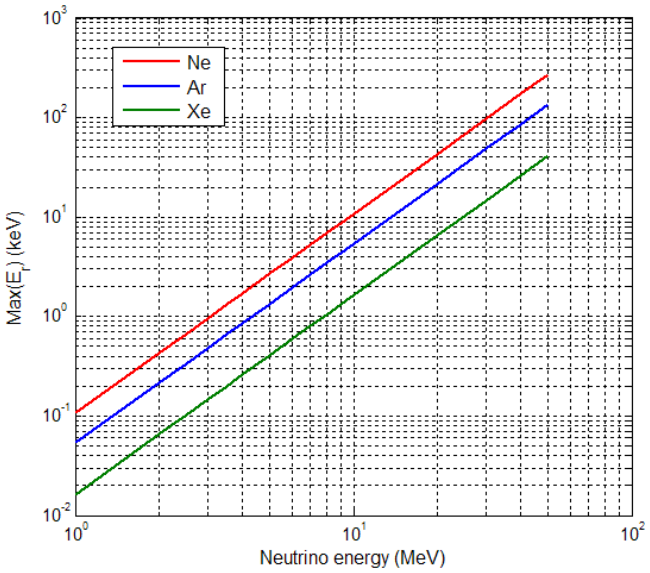

Figure 5.12: Maximum energy deposition in a coherent neutrino-nucleus scattering with different target species.

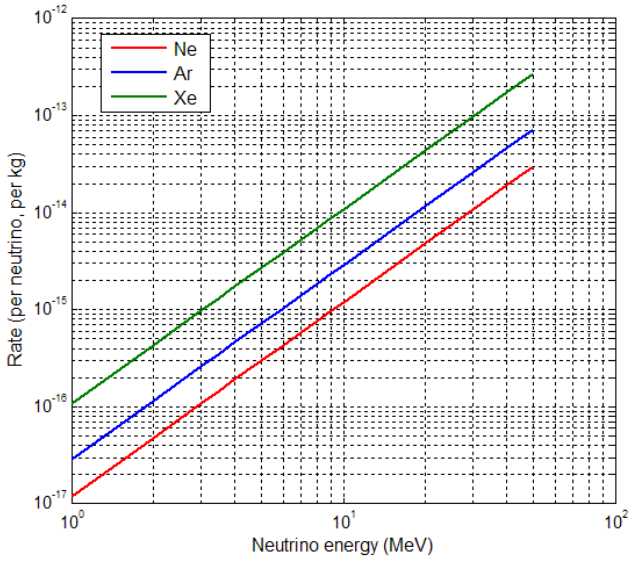

Figure 5.13: Expected count rate, computed from the quantities in figures 5.11 and 5.12. Note this is not an actual event rate: multiplication by the neutrino flux is required first.

, where N_t is the number of target atoms, E_{th} is the energy threshold of the detector, E_ν is the neutrino energy, Φ the neutrino flux, and σ the cross-section for CNS, given by equation 5.1. A complete calculation would include considerations about the energy threshold of the detector, which we will not do. In a simple calculation, the scattering rate can be approximated to:

$$R = N_t \Phi \sigma \tag{5.3}$$

The following table shows event rates calculated for ZEPLIN III. (Only the fiducial volume corresponding to the SE work is used, $\rho < 60\,mm$)

Table 5.1 shows neutrino fluxes provided from different sources. For the beta source, the geometry efficiency of the setup was considered to be 1/10. For solar ^8B and atmospheric neutrinos, the calculation shown gives an optimistic estimation for the event rate: equation (5.3) was used, even though both cases require

Neutrino source	$E_\nu\, MeV$	$\Phi\, cm^{-2}.s^{-1}$	$\sigma\, cm^2$	$R\, s^{-1}$	Events $/yr$
beta source (^{60}Co, $1Cu$)	0.31	3.7×10^8	7.7×10^{-42}	1.6×10^{-8}	0.49
sun, pep	1.442	1.41×10^8	3.6×10^{-41}	2.8×10^{-8}	0.87
sun, ^8B	20	3×10^6	5.0×10^{-40}	8.1×10^{-9}	2.6×10^{-1}
atmosphere	10	10^6	2.5×10^{-40}	1.35×10^{-9}	4.27×10^{-2}
near reactor	~ 3	5×10^{13}	7.5×10^{-41}	2.0×10^{-2}	6.4×10^5

Table 5.1: Tipycal neutrino fluxes with corresponding cross-sections, event rates and total number of events counted in a year of operation for ZEPLIN III

the integral calculation found in (5.2)), due to the continuum spectrum of neutrino energies. Nevertheless, the calculation made is a good exercise to show that both these natural sources are out of site for ZEPLIN III. On the other hand, the count rate found for reactor neutrinos might be interesting. The question is if this neutrino event rate is compatible with the spontaneous SE rate that was measured.

An important consideration that needs to be done is how many of these 6.4×10^5 events that we might expect in a year will produce two-electron signals, which will allow distinction from the noisy one-electron events. Ionization yield is fundamental for this calculation. Assuming $10\, e^-/keV$, reference [(33)] suggests that around 14% of the events will be two-electron (or more). From here, and recalling that the spontaneous event rate for the inner 60 mm radius is 13 Hz, one can estimate the number of neutrino and SE noise events after a one year run (figure 5.14).

The leakage is 117 events per year above threshold. To fight this leakage, it is important to have a high mean number of photoelectrons in the single electron cluster, because this will allow good distinction between one-electron and two-electron peaks. A low mean number of photoelectrons implies great overlap of one and two-electron peaks, making it impossible to exclude the one-electron peak without significant loss of two-electron statistics. Previous ZEPLIN II measured 8.8 ± 0.4 photoelectrons [(34)] and more recently, XENON10 collaboration has counted 24 ± 7 [(38)].

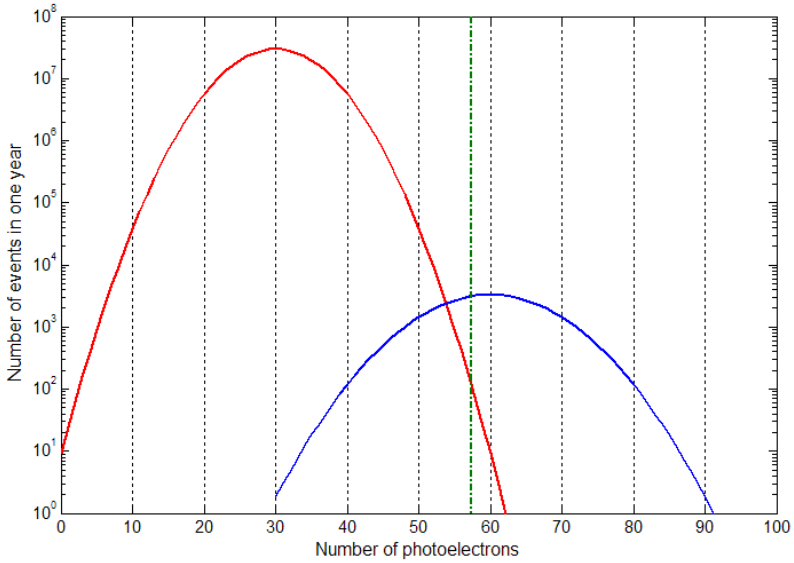

Figure 5.14: Number of events after one year run. The single-electron peak (red) is only due to spontaneous SE events in the detector. The blue curve is the two-electron peak from neutrino events. The dashed line shows the 5σ threshold above the mean of the SE distribution.

So, although a significant rate of spontaneous SE events was found in ZEPLIN III, the high mean number of photoelectrons in the SE signal ($\sim$31) maintains a window of opportunity opened for CNS searches. When looking for these interactions, the SE background could be excluded considering only two-electron (or more) signals.

Chapter 6

Prospects for Measurements of Xenon Response with Low-energy Ions

6.1 Objectives

As it has been stressed, good knowledge of the scintillation efficiency of liquid xenon for nuclear recoils in the low energy region is of primary importance for reliable determination of the energy deposited by a WIMP in the detector and, therefore, for setting the sensitivity limit of the experiment (or, if WIMP signal is detected, for measurement the energy spectrum and, finally, the WIMP mass). The existing data on $\mathcal{L}_{eff}$ are not consistent below $\sim$ 10 keV (see figure 3.3). Besides, all measurements have been done using the same technique - elastic scattering of neutrons off a liquid xenon target and due to that, they may suffer from a common systematic error, at present unknown. This fact inspired us to search for an alternative method of measuring the relative scintillation efficiency. In this section we explore the possibility of bombarding a xenon target with xenon ions from an ion accelerator. The major problem of this experiment is delivery of ions with the energy in the keV range to the target at high ($\sim$ 1 bar) gas pressure. For that it is proposed to use an extremely thin window of the order of 20 nm commercially available nowadays. The aspects to be studied are: 1) degradation of the energy spectrum of monochromatic ions on passage through the window;

2) angular dispersion of the emerging ions; 3) contamination of the emerging Xe beam with recoil nuclei of the window material as well as the electrons. Here, we consider the two first issues using SRIM software for calculations.

6.2 Existing Experience with Scintillation Crystals

In 2008, an measurement was made in the framework of the CRESST experiment [(39)], where solid $CaWO_4$ was the target material for ions with fixed kinetic energy. Light was detected using a photomultiplier.

With this example, one can think of reproducing an equivalent experiment for solid xenon. Indeed, the low vapor-pressure above frozen xenon would be a favorable medium for low-energy ions to pass undisturbed.

But several problems arise. Such an experiment with a solid target is sensible to surface effects, which can degrade the light output when energy depositions occur near the crystal surface. In the case of $CaWO_4$, such an effect was not observed, suggesting that bulk and surface have the same quenching factor. As for solid xenon, the sublimating surface can represent a problem. Moreover freezing xenon requires very low temperatures and might be a problem itself.

Finally, we must not forget that these hypothetical measurements in solid xenon would have to be meaningful for the liquid phase. The acceptance of this transition could be difficult, as in the liquid phase things might be different.

6.2.1 Simulation of the Ion Passage Through Si_3N_4 Windows

Other possibility is to confine liquid xenon, injecting ions through a thin window. The window will generate energy dispersion, momentum dispersion and injection of electrons and atoms from the window. These effects are studied in this section, using the simple geometry shown in figure 6.1.

Three different window thicknesses are explored, choosing ion energies that deliver an energy spectrum which is of interest, after crossing the window. In all

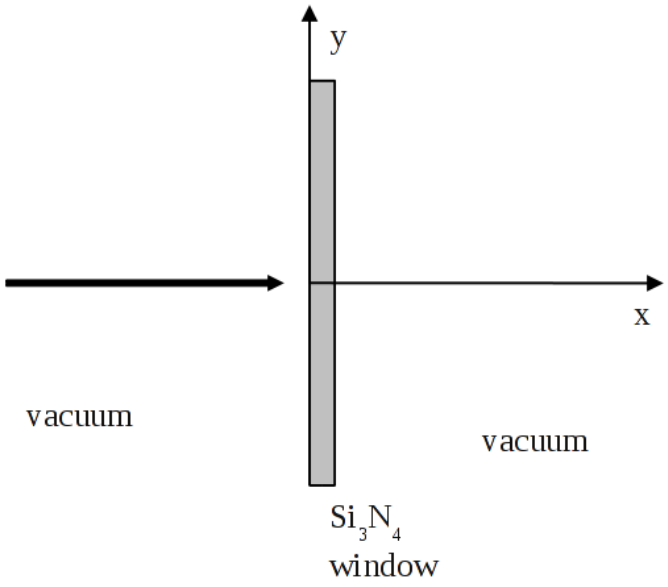

Figure 6.1: Schematic representation of the geometry of the simulation.

combinations of ion energy with window thickness, 10 000 ions were simulated. Transmission efficiency, energy spectrum of outgoing ions and respective momentum deflection from the initial ion beam direction are computed. Figures 6.2 to 6.7 show the results.

In every energy spectrum, the first bin shows a peak. Figure 6.4 is a detailed look into one of these distributions and shows no structure inside the first bin.

6.3 Conclusions

Choosing the thinnest window possible ($20nm$) will introduce the lower energy dispersion in the incoming ion beam. The PMT amplitude spectrum for an incoming ion beam whit a δ-function energy spectrum would be a direct measurement of the scintillation efficiency:

$$A = \mathcal{L}_{eff}(E)$$

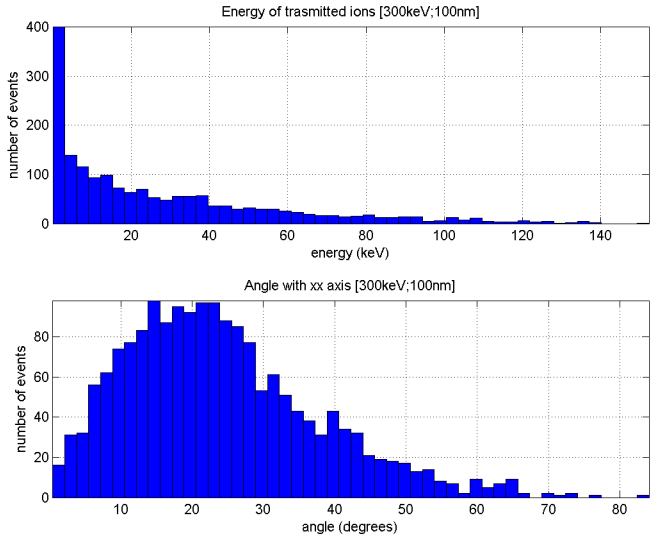

Figure 6.2: Energy and momentum dispersion for 300 keV Xe ion after transposing a 100 nm thick Si_3N_4 window. Transmission efficiency: 17.9%.

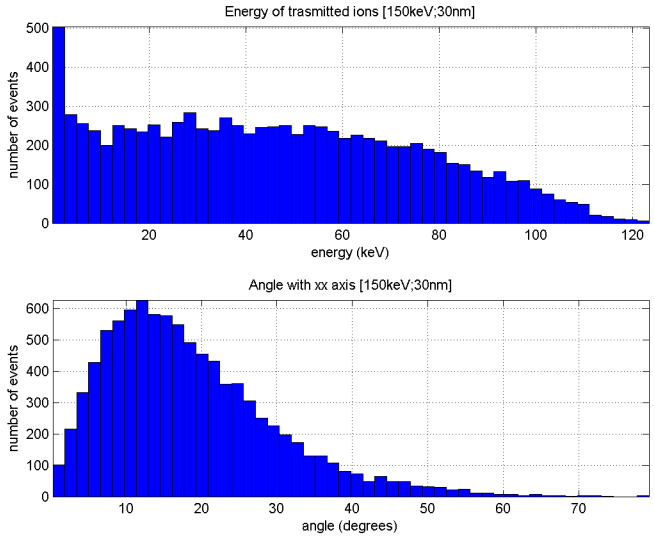

Figure 6.3: Energy and momentum dispersion for 300 keV Xe ion after transposing a 100 nm thick Si_3N_4 window. Transmission efficiency: 92.8%.

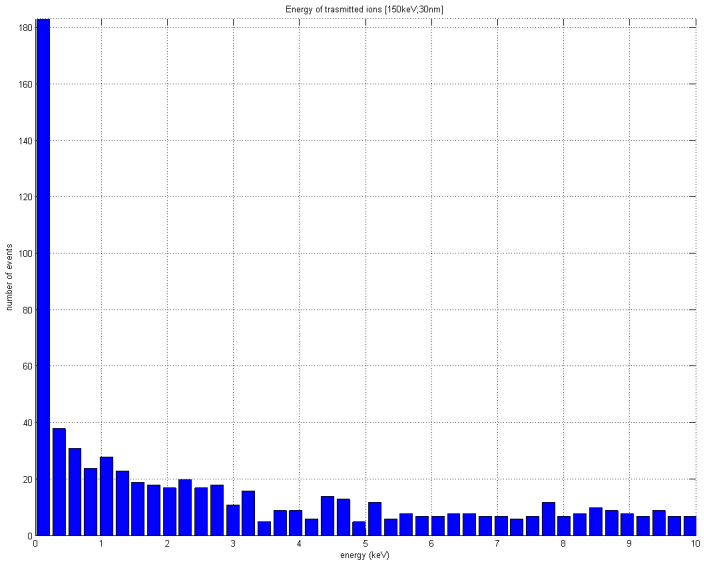

Figure 6.4: Energy dispersion for 150 keV Xe ion after transposing a 30 nm thick Si_3N_4 window (detail).

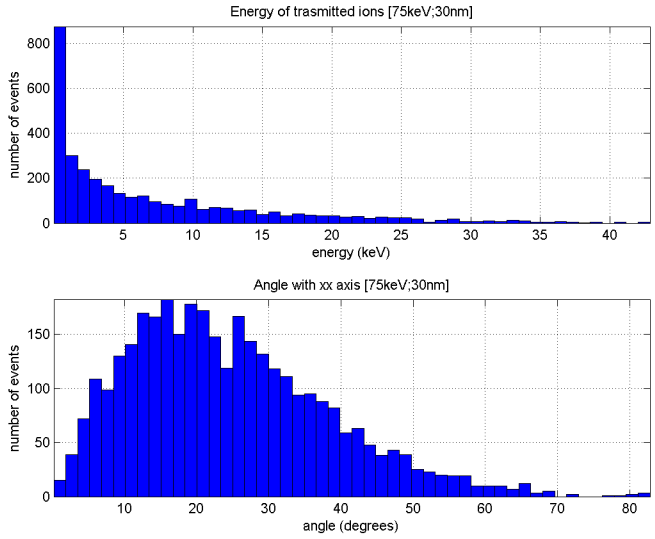

Figure 6.5: Energy and momentum dispersion for 75 keV Xe ion after transposing a 30 nm thick Si_3N_4 window. Transmission efficiency: 33.8%.

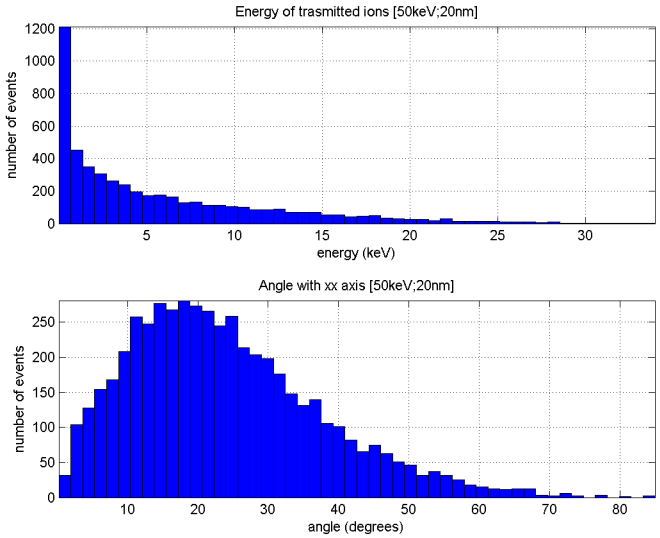

Figure 6.6: Energy and momentum dispersion for 50 keV Xe ion after transposing a 30 nm thick Si_3N_4 window. Transmission efficiency: 51.9%.

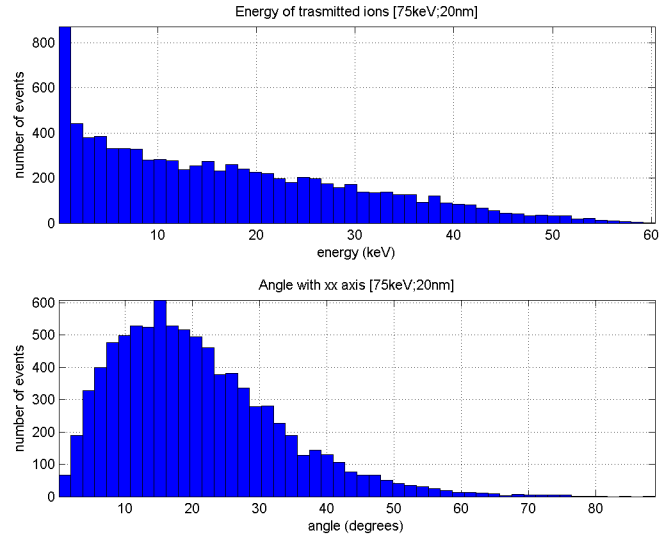

Figure 6.7: Energy and momentum dispersion for 75 keV Xe ion after transposing a 20 nm thick Si_3N_4 window. Transmission efficiency: 86.7%.

The window thickness will introduce energy dispersion, making necessary the convolution of the incoming energy spectrum with $\mathcal{L}_{eff}$:

$$A = \int f(E)\, \mathcal{L}_{eff}(E)\, dN$$

Chapter 7

Conclusion

In this work, the following aspects relevant to direct dark matter detection and search for coherent neutrino scattering with liquefied noble gas detectors have been studied.

1. The scintillation efficiency of liquid xenon (and to some extend of liquid argon) for nuclear recoils, which has direct impact on the energy scale calibration of those detectors, has been computed using GEANT4 Monte Carlo simulation package. Several models for screening functions have been used. The simulation has been validated for several particles (alpha-particles, argon and xenon ions) and stopping media (water, liquid argon and liquid xenon) by comparison with the respective results obtained with TRIM code. The simulation allowed the scintillation efficiency of liquid argon and xenon for respective nuclear recoils to be calculated being the results in good agreement with the existing experimental data.

2. The possibility of measuring the scintillation efficiency of liquid xenon for nuclear recoils by bombarding the liquid target with Xe ions has been explored. Specifically, the passage of low energy xenon ions through a 20 nm to 100 nm thick Si_3N_4 window has been studied using TRIM code. Energy spectra and angular distributions of the emerging Xe ions have been obtained. It has been shown that for the experiment to be feasible the energy distribution of the ions after the passage through the window must be very well described. If successful,

such experiment would provide an independent measurement of the scintillation efficiency of liquid targets for low energy ions with a new technique, different from that used until now.

3. Secondary scintillation signals due to spontaneously produced single electrons in the liquid xenon target of the ZEPLIN-III dark matter detector were analysed. Their amplitude distribution, timing properties and spatial distribution across the liquid were obtained. It was found that a single electron emerging from the liquid xenon in ZEPLIN-III produces 31.1 ± 0.2 photoelectrons on the photocathodes of the photomultipliers, in total. The photomultiplier amplitude spectrum is well described with a gaussian function with sigma of 7.8 photoelectrons. This shows high sensitivity and good resolution of the detector for extremely low ionisations (a few electrons) especially important for future experiments on coherent neutrino scattering. The obtained results also indicate relatively high rate ($\sim$ 13 Hz) of spontaneous emission of single electrons, which takes place both in the bulk of the liquid and from the surface of the wire grid kept at high voltage. This spontaneous electron emission will constitute background for the neutrino experiments although does not have a significant impact in the case of dark matter search.

Appendix A

Appdx A

A.1 Ziegler's Scientific Citations for Xenon

These are Zieglers's collected scientific citations for xenon. They are only complete untill the year 2003. At the date of this writing, these citations are lacking in the public website and are presented here in the interest of the reader.

Citations for Target : Xe

Pub. Year	Authors, Title, Journal Citation and Comments	Citation Numb
1924	Bates, L. F. **'On the Range of Alpha-Particles in Rare Gases'** ***Proc. Roy. Soc., A106, 622-632 (1924)*** *Comment : R. 6.1-MeV He -> He, Ne, O2, Ar, Kr, Xe*	**1924-Bate** 0010
1925	Gurney, R. W. **'The Stopping-Power of Gases for Alpha-Particles of Different Velocities'** ***Proc. Roy. Soc., A107, 340-349 (1925)*** *Comment : S. 5.3, 6.1 MeV He -> H2, He, O2, Ne, Ar, Kr, Xe Rel. To Air*	**1925-Gurn** 0061
1934	Naidu, R. **'Sur Les Courbes D'Ionisation Des Rayons Alpha Du Polonium Dans Les Gaz Rares'** ***J. Phys. Radium, 5, 575-77 (1934)*** *Comment : S. 3-7 MeV He -> He, Ne, Ar, Kr, Xe. All Rel. To Air*	**1934-Naid** 0093
1934	Naidu, R. **'Courbes D'Ionisation Dans Les Krypton Et Le Xenon Purs Relatives Aux Rayons Alpha Du Polonium'** ***J. Phys. Radium, 5, 343-46 (1934)*** *Comment : R. 5.3 MeV He -> Kr, Xe*	**1934-Naid2** 0511
1953	Reynolds, H. K. Dunbar, D. N. F. Wenzel, W. A. Whaling, W. **'The Stopping Cross Section of Gases for Protons, 30-600 keV'** ***Phys. Rev., 92, 742-48 (1953)*** *Comment : S. 30-600 keV H -> H2, He, O2, Air, N2, Ne, Ar, Kr, Xe, Hydrocarbons.*	**1953-Reyn** 0103
1954	Chilton, A. B. Cooper, J. N. Harris, J. C. **'The Stopping Power of Various Elements for Protons of Energies from 400 to 1050 keV'** ***Phys. Rev., 93, 413-18 (1954)*** *Comment : S. 400-1050 keV H -> N2, Ne, Ar, Kr, Xe, Ni, Cu*	**1954-Chil** 0032
1955	Brolley, J. E. Ribe, F. L. **'Energy Loss by 8.86 MeV Deuterons and 4.43 MeV Protons.'** ***Phys. Rev., 98, 1112-14 (1955)*** *Comment : S. 4.43 MeV H -> H2, Air, Kr. 8.86 MeV D -> H2, He, N2, O2, Ne, Ar, Kr, Xe*	**1955-Brol** 0026
1955	Riezler, U. Rudloff, A. **'Ionisation und Energieverlust von Alpha-Teilchen in Verschiedenen Gasen'** ***Ann. Physik, 18, 224-245 (1955)*** *Comment : R. S Rel. To Air. 5.3 MeV He -> He, Ne, Ar, Kr, Xe, H2, N2, O2, NH3, CO, CO2, NO, N2O, CH4, C2H6, C3H8, C4H10*	**1955-Riez** 0567
1959	Rousset, A. Lagarrique, A. Musset, P. Rancon, P. Santeron, X. **'Relativistic Increase of Ionization in Xenon'** ***Nuovo Cimento, 14, 365-75 (1959)*** *Comment : S. 0.5-50 GeV/c Mu -> Xe, Xe + He Rel. To Min.*	**1959-Rous** 0120

Citations for Target : Xe

Pub. Year	Authors, Title, Journal Citation and Comments	Citation Numb
1963	Wolke, R. L. Bishop, W. N. Eichler, E. Johnson, N. R. O'Kelley, G. D. **'Ranges and Stopping Cross Sections of Low-Energy Tritons'** ***Phys. Rev., 129, 2591-96 (1963)*** *Comment : R, S. 0.2-2.73 MeV T -> N2, Al, Ar, Ni, Kr, Xe.*	**1963-Wolk** 0142
1964	Gilat, J. Alexander, J. M. **'Stopping of Dysprosium Ions in Gases and Al'** ***Phys. Rev. B, 136, 1298-1305 (1964)*** *Comment : R. 6-21 MeV Dy -> He, N2, Ne, Ar, Kr, Xe*	**1964-Gila** 0185
1966	Mason, D. L. Prior, R. M. Quinton, A. R. **'The Energy Straggling of 1 MeV Protons in Gases'** ***Nucl. Inst. Methods, 45, 41-44 (1966)*** *Comment : dS. 1 MeV H -> H, He, N, O, Ar, Xe*	**1966-Maso** 0282
1968	Cano, G. L. **'Total Ionization and Range of Low-Energy Recoil Particles in Pure and Binary Gases'** ***Phys. Rev., 169, 277-79 (1968)*** *Comment : R. 103 keV 206Pb -> Ne, Ar, Xe, N2, Air, Hydrocarbons*	**1968-Cano** 0331
1968	Hvelplund, P. **'Prisopgave'** ***Aarhus University P. 1-105 (In Danish) (1968)*** *Comment : S, dS. Many Ions (H-Hg) at 50-500 keV -> H, He, Ne, Ar, Kr, Xe, Air*	**1968-Hvel** 0406
1969	Ramirez, J. J. Prior, R. M. Swint, J. B. Quinton, A. R. Blue, R. A. **'Energy Straggling of Alpha Particles through Gases'** ***Phys. Rev., 179, 310-14 (1969)*** *Comment : S, dS. 1-3.5 MeV He -> He, Air, Ar, Kr, Xe*	**1969-Rami** 0388
1971	Chu, W. K. Powers, D. **'Energy Loss of Alpha Particles in Noble Gases from 0.3 - 2.0 MeV'** ***Phys. Rev. B, 4, 10-15 (1971)*** *Comment : S. 0.3-2.0 MeV He -> He, Ne, Ar, Kr, Xe*	**1971-Chu** 0675
1971	Hakim, M. Schafrir, N. H. **'252Cf Fission Fragment Energy Loss Measurements in Elementary Gases and Solids as Compared with Theory'** ***Can. J. Phys., 49, 3024-35 (1971)*** *Comment : S. Fiss. Fragm. -> H2 D2, He, C, N2 O2, Ne, Al, Ar, Ni, Cu, Kr, Ag, Xe, Au*	**1971-Haki** 0432
1971	Leon, J. Steiger-Shafrir, N. H. **'Range and Range Straggling of 97 keV 224Ra Particles in Gases'** ***Can. J. Phys., 49, 1004-17 (1971)*** *Comment : R, dR. 97 keV 224Ra -> H2, He, N2, O2, Ne, Ar, Kr, Xe*	**1971-Leon** 0446

Citations for Target : Xe

Pub. Year	Authors, Title, Journal Citation and Comments	Citation Numb
1971	Pierson, W. R. Kummer, J. T. Brachuczek, W. **'Ranges of Recoil Atoms from the (n,gamma) Process'** ***Phys. Rev. B, 4, 2846-53 (1971)*** *Comment : R. About 50 eV Au -> D, He, Ne, Ar, Xe*	**1971-Pier** 0458
1972	Huetter, G. T. Madey, R. Yushak, S. M. **'Fluctuations in the Energy Loss of 66- and 100-MeV Protons in a Thin Proportional Counter'** ***Phys. Rev. A, 6, 250-55 (1972)*** *Comment : dS. 66, 100 MeV H -> (0.9 Xe, 0.1 CH4)*	**1972-Huet** 0467
1975	Sidenius, G. Andersen, N. **'Multiple Scattering of keV Ions' Lateral Distributions in Argon and Nitrogen'** ***Nucl. Inst. Methods, 131, 387-389 (1975)*** *Comment : dR (lateral). (50-180 keV) H, He, N, Ne, Ar -> Ar, N, Xe*	**1975-Side** 1261
1977	Andersen, H. H. Besenbacher, F. Knudsen, H. **'Stopping Power and Straggling of 65 - 500 keV Lithium Ions in H2, He, CO2, N2, O2, Ne, Ar, Kr, and Xe'** ***Nucl. Inst. Methods, (1977) -b*** *Comment : S, dS. 65 - 500 keV Li -> H2, He, CO2, N2, O2, Ne, Ar, Kr, Xe*	**1977-Ande4** 0930
1977	Besenbacher, F. **'Stopping Power and Straggling for H and He Ions in Gas Targets'** ***Specialeopgave. Aarhus University (1977)*** *Comment : S. dS. 20-500 keV H, He -> H, He N, O, Ne, Ar, Kr, Xe, CO2*	**1977-Bese** 0954
1978	Andersen, H. H. Besenbacher, F. Knudsen, H. **'Stopping Power and Straggling of 65-500 keV Lithium Ions in H, He, CO, N, O, Ne, Ar, Kr and Xe'** ***Nucl. Inst. Methods, 149, 121-127 (1978)*** *Comment : S. Li (65-500 keV) -> H, He, CO2, N, O, Ne, Ar, Kr, Xe*	**1978-Ande** 1492
1979	Besenbacher, F. Andersen, H. H. Hvelplund, P. Knudsen, H. **'Stopping Power of Swift Hydrogen and Helium Ions in Gases'** ***Kgl. Danske Videnskab. Selskab Mat. Fys. Medd. 40, 1-39 (1979)*** *Comment : S. 40 keV-1 MeV H And 100 keV-2.4 MeV He -> H2, He, N2, O2, CO2, Ne, Ar, Kr, Xe*	**1979-Bese** 1160
1979	Dennis, J. A. Powers, D. **'The Dependence of Stopping Power on Physical and Chemical States'** ***Preprint (1979) 8*** *Comment : S. H, He -> Gases (Review Of Current Data)*	**1979-Denn** 1193
1980	Besenbacher, F. Andersen, J. U. Bonderup, E. **'Straggling in Energy Loss of Energetic Hydrogen and Helium Ions'** ***Nucl. Inst. Methods, 168, 1 (1980)*** *Comment : R, dR. 0-600 keV H, He -> Ar, Ne, Kr, Xe, Ni, Au, Ag, Al*	**1980-Bese** 1353

Citations for Target : Xe

Pub. Year	Authors, Title, Journal Citation and Comments	Citation Numb
1981	Fukuda, A. **'Stopping Powers in Rare Gases for 40-200 keV Rare-Gas Ions'** ***J. Phys. B, Atom. and Molec. Phys.,14, 4533-4544 (1981)*** *Comment : S. He, Ne, Ar, Kr (40-200 keV) -> He, Ne, Ar, Kr, Xe (Note: stopping for ions of zero deflection)*	**1981-Fuku** 1411
1982	Geissel, H. Laichter, Yl Schneider, W. F. W. Armbruster, P. **'Energy Loss and Energy Loss Straggling of Fast Heavy Ions in Matter'** ***Nucl. Inst. Methods, 194, 21-29 (1982)*** *Comment : S. Heavy Ions (18 - 92) at 0.5-10 MeV/amu -> 17 Solids and 5 Gases*	**1982-Geis** 1417
1982	Laichter, Y. Geissel, H. Shafrir, N. H. **'On the Nuclear Charge and Atomic Mass of Attenuated Mean Fission Fragments'** ***Nucl. Inst. Methods, 194, 45-50 (1982)*** *Comment : S. Fission Frag. (from Cr, U) -> N, Ne, Ar, Cr, Xe*	**1982-Laic2** 2002
1983	Baumgart, H. Arnold, W. Berg, H. Huttel, E. Clausnitzer, G. **'Proton Stopping Powers in Various Gases'** ***Nucl. Inst. Methods, 204, 597 (1983)*** *Comment : H (60-800 keV) -> H, He, N, O, Ne, Ar, Kr, Xe*	**1983-Baum** 1614
1983	Baumgart, H. Berg, H. Huttel, E. Pfaff, E. Reiter, G. **'He4 Stopping Cross Sections in H2, He, N2, O2, Ne, Ar, Kr, Xe, CH4 and CO2'** ***Nucl. Inst. Methods, 215, 319-328 (1983)*** *Comment : S. He (0.1-1.2 MeV) -> H2, He, N2, O2, Ne, Ar, Kr, Xe, CH4 and CO2*	**1983-Baum3** 1450
1983	Herold, W. D. Egger, J. Kaspar, H. Pocar, F. **'Precision Measurements of Energy Loss Distributions in Xenon Using Proportional Scintillation in a Wire Chamber'** ***Nucl. Inst. Methods, 217, 277 (1983)*** *Comment : S. Pions (60-285 MeV) -> Xe*	**1983-Hero** 1662
1983	Laichter, Y. Shafrir, N. H. **'Fine Structure in the Stopping Powers and Ranges of Fission Fragments in Matter'** ***Nucl. Phys., A394, 77-86 (1983)*** *Comment : S. Fission fragments (Cf-252) -> H, D, He, N, O, Ne, Ar, Kr, Xe*	**1983-Laic** 1696
1988	Herault, J. Bimbot, R. Gauvin, H. Anne, R. Bastin, G. **'Interaction of 20-100 MeV/amu Heavy Ions with Cold Matter'** ***J. Physique Coll., 49C, 7-33 (1988)*** *Comment : S. O, Ar, Ca, Kr, Mo, Xe (24-95 MeV/amu) -> Ne, Ar, Kr, Xe, CH4, C4H10, N, CO2, CF4, Be, Al, Si, Ti, Ni, Cu, Ag, Ta, Au*	**1988-Hera** 1972

Citations for Target : Xe

Pub. Year	Authors, Title, Journal Citation and Comments	Citation Numb
1989	Bimbot, R. Cabot, C. Gardes, H. Orliange, I. **'Stopping Power of Gases for Heavy Ions: Gas-Solid Effect II. 2-6 MeV/amu Cu, Kr and Ag Projectiles'** ***Nucl. Inst. Methods, B44, 19-34 (1989)*** *Comment : S. Cu, Kr, Ag (2-5 MeV/amu) -> H, He, N, O, Ne, Ar, Kr, Xe (11 gases)*	**1989-Bimb** 1934
1989	Bimbot, R. Cabot, C. Gardes, D. Gauvin, H. Hingmann, R. **'Stopping Power of Gases for Heavy Ions: Gas-Solid Effects I. 2-13 MeV/amu Ne and Ar Projectiles'** ***Nucl. Inst. Methods, B44, 1-18 (1989)*** *Comment : S. Ne, Ar (2-13 MeV/amu) -> H, He, N, O, Ne, Ar, Kr, Xe (12 gases)*	**1989-Bimb2** 1935
1989	Bimbot, R. Gauvin, H. Herault, J. Anne, R. Bastin, G. **'Interaction of 20-100 MeV/amu Heavy Ions with Solids and Gases'** ***Rad. Effects, 110, 15-17 (1989)*** *Comment : S. O, Ar, Ca, Kr, Mo, Xe (20-95 MeV/amu) -> 10 Gases, 12 Solids*	**1989-Bimb3** 1936
1990	Reiter, G. Kniest, N. Pfaff, E. Clausnitzer, G. **'Proton and Helium Stopping Cross Sections in H, He, N, O, Ne, Ar, Kr, Xe, CH4'** ***Nucl. Inst. Methods, B44, 399-411 (1990)*** *Comment : S. H, He (0.7-3.0 MeV) -> H, He, N, O, Ne, Ar, Kr, Xe, CH4*	**1990-Reit** 1933
1991	Herault, J. Bimbot, R. Gauvin. H. Kubica, B. Anne, R. **'Stopping Powers of Gases for Heavy Ions (O, Ar, Kr, Xe) at Intermediate Energy (20-100 MeV.amu). Vanishing of the Gas-Solid Effect'** ***Nucl. Inst. Methods, B61, 156-166 (1991)*** *Comment : S. O, Ar, Kr, Xe (20-85 MeV/amu) -> He, O, N, (11 gases)*	**1991-Hera** 1908
1993	Novkovic, D. Subotic, K. Milosevic, Z. Manic, S. Stojanovic, M. **'Alpha Particle Energy Straggling Measurements in Nobel Gases'** ***J. Moscow Phys. Soc. (UK), 3, 215-220 (1993)*** *Comment : dS. He(8.8 MeV) -> He, Ne, Ar, Kr, Xe*	**1993-Novk** 2077
1993	Price, J. L. Simons, D. G. Stern, S. H. Land, D. J. Guardala, N. A. **'Stopping Powers of the Noble Gases for 0.3-10.0 MeV Nitrogen Ions'** ***Phys. Rev. A, 47, 2913-2918 (1993)*** *Comment : S. N (0.3-10.0 MeV) -> He, Ne, Ar, Kr, Xe*	**1993-Pric** 1873
1996	Bimbot, R. Barbey, S. Benfoughal, T. Clapier, F. Mirea, M. **'Stopping Powers of Gases for Very Heavy Ions'** ***Nucl. Inst. Methods, B107, 9-14 (1996)*** *Comment : S. U, Pb (24 MeV/amu, 29 MeV/amu) -> H, N, O, N, Ar, Kr, Xe*	**1996-Bimb** 1828
1996	Fukuda, A. **'Stopping Powers of the Rare Gases for 50-200 keV N+ Ions'** ***J. Phys. B, 29, 3717-3725 (1996)*** *Comment : S. N (50-200 keV) -> He, Ne, Ar, Kr, Xe,*	**1996-Fuku** 1642

Citations for Target : Xe

Pub. Year	Authors, Title, Journal Citation and Comments	Citation Numb
2001	Diwan, P. K. Kumar, S. Singh, G. Singh, L. **'Energy Loss of Heavy Ions in Gases: A Comparative Study'** ***Rad. Meas., 33, 193-202 (2001)*** *Comment : S. Ne, S,Cl,Ar,Cu,Kr (1 - 80 MeV/u) -> H,He, N,Ar,Ne,Xe,CH4,C4H10,CO2,CF4*	**2001-Diwa2** 2369

Appendix B

Appdx B

B.1 Nuclear Screening Functions

The simplest screening function is given by Bohr:

$$\Phi_{Bohr} = \exp\left(-\frac{r}{a_0}\right) = \exp\left(-x\right)$$

, where the Bohr radius is $a_0 = \hbar^2/me^2 = 0.529$.
But there are other screening functions that have been sugested over the years. They are always described by defining a reduced radius (x) from a screening lengh a_i, as $x \equiv r/a_i$. The G4ScreenedNuclearRecoil class is prepared to use the following screening functions, according to the users will.

B.1.1 Moliere Screening

Moliere evaluated the Thomas Fermi atom and found a function that includes exponencial decay.

$$\phi_{Moliere} = 0.35\exp\left(-0.3x\right) + 0.55\exp\left(-1.2x\right) + 0.1\exp\left(-6.0x\right)$$

, with

$$a_U = \frac{0.8853 \times a_0}{\sqrt{Z_1^{\frac{2}{3}} + Z_2^{\frac{2}{3}}}}$$

B.1.2 Lenz-Jensen Screening

This is another classical screening function:

$$\phi_{LJ} = 0.7466 \exp(-1.038x) + 0.2433 \exp(-0.3876x) + 0.01018 \exp(-0.206x)$$

, with

$$a_U = \frac{0.8853 \times a_0}{\sqrt{Z_1^{\frac{2}{3}} + Z_2^{\frac{2}{3}}}}$$

B.1.3 ZBL Screening

$$\phi_U = 0.1818 \exp(-3.2x) + 0.5099 \exp(-0.9423x) +$$

$$+0.2802 \exp(-0.4028x) + 0.02817 \exp(-0.2016)$$

, with

$$a_U = \frac{0.8853 \times a_0}{Z_1^{0.23} + Z_2^{0.23}}$$

B.1.4 LJZBL Screening

LJZBL is a hybrid screening function. It uses LJ screening if $x < 0.25 * a_{univ}$ and ZBL if $x > 1.5 * a_{univ}$, with a connector in between.

Appendix C

Appdx C

C.1 Effective Charge Calculation

The effective charge of an ion transposing the detection medium is computed from the charge of the stripped atom (z_i) according to

$$z_{eff} = \gamma_i z_i$$

where, for heavy ions

$$\gamma_i = \left(q + \frac{1-q}{2} \left(\frac{v_0}{v_F} \right)^2 \ln\left(1 + \Lambda^2\right) \right) \left(1 + \frac{(0.18 + 0.0015Z) \exp\left(-(7.6 - Q)^2\right)}{z_i^2} \right)$$

Here, q is the fractional average charge of the ion, v_0 is the Bohr velocity, v_F is the Fermi velocity of the electrons in the target medium, and Λ is a term accouting for the screening effect:

$$\Lambda = 10 \frac{v_F}{v_0} \frac{(1-q)^{2/3}}{z_i^{1/3}(6+q)}$$

The Fermi velocity of the medium will depend on the detailed electronic structure of the atoms that build it. As for the fractional average charge of the ion, it is delivered by the expression

$$q = \left[1 - \exp\left(0.803y^{0.3} - 1.3167y^{0.6} - 0.38157y - 0.008983y^2\right)\right]$$

where y is a function of the ion velocity v_i:

$$y = \frac{v_i}{v_0 Z^{2/3}} \left(1 + \frac{v_F^2}{5v_i^2}\right)$$

References

[1] K. Masuda T. Doke. Present status of liquid rare gas scintillation detectors and their new application to gamma-ray calorimeters. *Nucl. Instr. Meth. A*, 420, 1999. x, 31

[2] K.-H. Chae et al. Constraints on cosmological parameters from the analysis of the cosmic lens all sky survey radio-selected gravitational lens statistics. *Phys. Rev. Lett.*, 89(15), 2002. 3

[3] Martin Elvis et al. The chandra cosmos survey. i. overview and point source catalog. *ApJS*, 184:158, 2009. 3

[4] C. Alcock et al. Theory of exploring the dark halo with microlensing. i. power-law models. *ApJ*, 449(28), 1995. 3

[5] V. Rubin and W.K. Ford. Rotation of the andromeda nebula from a spectroscopic survey of emission regions. *Astrophys. J.*, 159:379, 1970. 6

[6] G. Servant and T. M. P. Tait. *Nucl. Phys. B*, 650(391), 2003. 17

[7] KJMč. Axions, inflation and the anthropic principle. submitted to Physical Review D, (arXiv:0911.0421), 2009. 17

[8] KJM & P.J. Steinhardtč. Cosmological problems with multiple axion-like fields. submitted to Physical Review D, (arXiv:0911.0418), 2009. 17

[9] P. Benetti et al. *NIM A*, 329:361, 1993. 19

[10] M. Ageron et al. Performance of the first antares detector line. *Astroparticle Phys*, 31(4):277–283, 2009. 19

[11] R. Gaitskell. *Rev. Nucl. Part. Sci*, 54:315–359, 2004. 21

[12] T. Morlat F. Giuliani and T. A. Girard. Heavy superheated droplet detectors as a probe of spin-independent wimp dark matter existence. *Phys. Rev. D*, 75(6), 2007. 22

[13] A. Davour. The picasso dark matter search project. *Proc. of Identification of Dark Matter 2008*, 2008. 22

[14] T. Morlat TA Girard F. Giuliani M. Felizardo da Costa R.C. Martins, A.R. Ramos and J.G. Marques. New acoustic instrumentation for the simple superheated droplet detector. *Nucl. Instr. Meth. A*, 589(72), 2008. 22

[15] Alexander I. Bolozdynya E. Aprile, Aleksey E. Bolotnikov and Tadayoshi Doke. *Noble Gas Detectors*. WILEY-VCH, 2006. 23

[16] G. Arnison et al. G. Alner, H. Araújo. Performance of the first antares detector line. *Astroparticle Phys*, 23:444462, 2005. 23

[17] A. Bewick et al. G. Alner, H. Araújo. *Astroparticle Phys*, 28:287302, 2007. 23

[18] H. Araújo et al. D. Akimov, G. Alner. *Astroparticle Phys*, 27:4660, 2007. 23

[19] F. Arneodo et al. J. Angle, E. Aprile. *Phys. Rev. Let.*, 100(2), 2008. 23

[20] XENON Collaboration: Elena Aprile. The xenon dark matter experiment. *ArXiv Astrophysics e-prints*, 2005. 23

[21] A. Rubbia. Ardm: a ton-scale liquid argon experiment for direct detection of dark matter in the universe. *Journal of Physics Conference Series*, 39:129–132, 2006. 23

[22] V. Chepel M. I. Lopes. *Electronic Excitations in Liquified Rare Gases, chapter 11 - Rare Gas Liquid Detectors*. ASP, 2005. 26

[23] F. Arneodo et al. Determination of through-going tracks' direction by means of delta-rays in the icarus liquid argon time projection chamber. *Nucl. Instr. and Meth. in Phys. Res. A*, 449:147–157, 2000. 30, 36

[24] V. Chepel et al. Scintillation efficiency of liquid xenon for nuclear recoils with the energy down to 5 kev. *Astropart. Phys*, 26(58), 2006. 30

[25] J. Lindhard. *Mat.Fys. Medd. K. Dan. Vidensk. Selsk.*, 33(1), 1963. 32, 34

[26] J.B. Birks. *Proc. Phys. Soc. A*, 64:511, 1951. 32, 36

[27] Jay A. LaVerne et al. *Phys. Rev. B*, 54:15724, 1996. 36

[28] M. H. Mendenhall and R. Weller. An algorithm for computing screened coulomb scattering in geant4. *Nucl. Instr. Meth. B*, 227:420–430, 2005. 39

[29] W.-M. Yao et al. *Jour. of Phys.*, G33, 2006. 40

[30] 40, 41

[31] A.C.-Fonseca et al. Proceedings of the ieee nuclear science symposium and medical imaging conference. *Linear Algebra Appl.*, 572, October 18, 2004. 49

[32] H.M.Araújo et al. The zeplin iii dark matter detector: performance study using an end-to-end simulation tool. *Astroparticle Phys*, 26:140–153, 2006. 49

[33] D. Akimov. Detection of reactor antineutrino coherent scattering off nuclei with a two-phase noble gas detector. arXiv:0903.4821v1, 2009. 55, 63

[34] B. Edwards et al. et al. Measurement of single electron emission in two-phase xenon. *Astroparticle Phys*, 30:54–57, 2008. 57, 63

[35] U.Sowada W.F.Schmidt G.Bakale. *J. Phys. Chem.*, 80(23):2556, 1976. 58

[36] Jocelyn Monroe. Neutrino backgrounds to dark matter searches. *Phys. Rev. D*, 76, 2007. 60

[37] C. Hagmann and A. Berstein. Two-phase emission detector for measuring coherent neutrino nucleus scattering. *IEEE Trans. Nucl. Sci.*, 51:2151–2155, 2004. 60

[38] P. Sorensen et al. The scintillation and ionization yield of liquid xenon for nuclear recoils. *Nucl. Instrum. Meth.*, pages 339–346, 2009. 63

[39] J. Ninkovic et al. New technique for the measurement of the scintillation efficiency of nuclear recoils. submitted to NIM A (arXiv: astro-ph/0604094v1), 2008. 67